NASA/TM-20210016661

Updated Assessment of Turboelectric Boundary Layer Ingestion Propulsion Applied to Single-Aisle Commercial Transport

James L. Felder, Michael T. Tong, Sydney L. Schnulo, Jeffrey J. Berton,
Robert P. Thacker, and William J. Haller
Glenn Research Center, Cleveland, Ohio

Jason Kirk and Mark D. Guynn
Langley Research Center, Hampton, Virginia

NASA STI Program . . . in Profile

Since its founding, NASA has been dedicated to the advancement of aeronautics and space science. The NASA Scientific and Technical Information (STI) Program plays a key part in helping NASA maintain this important role.

The NASA STI Program operates under the auspices of the Agency Chief Information Officer. It collects, organizes, provides for archiving, and disseminates NASA's STI. The NASA STI Program provides access to the NASA Technical Report Server—Registered (NTRS Reg) and NASA Technical Report Server—Public (NTRS) thus providing one of the largest collections of aeronautical and space science STI in the world. Results are published in both non-NASA channels and by NASA in the NASA STI Report Series, which includes the following report types:

- TECHNICAL PUBLICATION. Reports of completed research or a major significant phase of research that present the results of NASA programs and include extensive data or theoretical analysis. Includes compilations of significant scientific and technical data and information deemed to be of continuing reference value. NASA counter-part of peer-reviewed formal professional papers, but has less stringent limitations on manuscript length and extent of graphic presentations.

- TECHNICAL MEMORANDUM. Scientific and technical findings that are preliminary or of specialized interest, e.g., "quick-release" reports, working papers, and bibliographies that contain minimal annotation. Does not contain extensive analysis.

- CONTRACTOR REPORT. Scientific and technical findings by NASA-sponsored contractors and grantees.

- CONFERENCE PUBLICATION. Collected papers from scientific and technical conferences, symposia, seminars, or other meetings sponsored or co-sponsored by NASA.

- SPECIAL PUBLICATION. Scientific, technical, or historical information from NASA programs, projects, and missions, often concerned with subjects having substantial public interest.

- TECHNICAL TRANSLATION. English-language translations of foreign scientific and technical material pertinent to NASA's mission.

For more information about the NASA STI program, see the following:

- Access the NASA STI program home page at http://www.sti.nasa.gov

- E-mail your question to help@sti.nasa.gov

- Fax your question to the NASA STI Information Desk at 757-864-6500

- Telephone the NASA STI Information Desk at 757-864-9658

- Write to:
  NASA STI Program
  Mail Stop 148
  NASA Langley Research Center
  Hampton, VA 23681-2199

NASA/TM-20210016661

![NASA logo]

Updated Assessment of Turboelectric Boundary Layer Ingestion Propulsion Applied to Single-Aisle Commercial Transport

James L. Felder, Michael T. Tong, Sydney L. Schnulo, Jeffrey J. Berton,
Robert P. Thacker, and William J. Haller
Glenn Research Center, Cleveland, Ohio

Jason Kirk and Mark D. Guynn
Langley Research Center, Hampton, Virginia

National Aeronautics and
Space Administration

Glenn Research Center
Cleveland, Ohio 44135

October 2022

Level of Review: This material has been technically reviewed by technical management.

Updated Assessment of Turboelectric Boundary Layer Ingestion Propulsion Applied to Single-Aisle Commercial Transport

James L. Felder, Michael T. Tong, Sydney L. Schnulo,
Jeffrey J. Berton, Robert P. Thacker, and William J. Haller
National Aeronautics and Space Administration
Glenn Research Center
Cleveland, Ohio 44135

Jason Kirk and Mark D. Guynn
National Aeronautics and Space Administration
Langley Research Center
Hampton, Virginia 23666

Summary

Recent advances in technology and a push for more environmentally friendly air transportation has led to interest in electrified aircraft propulsion (EAP). EAP encompasses many different propulsion system architectures, which can also enable new, synergistic propulsion-airframe integration approaches. This report contains a comprehensive update of a 2016 evaluation of the 154-seat single-aisle turboelectric aircraft with aft boundary layer propulsion (STARC–ABL) concept that uses a turboelectric EAP system to drive a fuselage boundary layer ingestion (BLI) propulsor. The predicted fuel consumption benefits of STARC–ABL are updated with cruise Mach number increased from 0.7 to 0.785 using updated and corrected analysis methodologies. Additionally, certification noise is added to the concept evaluation. To properly assess the impact of EAP, the single-aisle transport aircraft with aft boundary layer propulsion, or ST–ABL, concept is developed for comparison. The ST–ABL uses the same fuselage BLI propulsor as the STARC–ABL with the EAP system replaced by a tail-mounted turboshaft engine that drives the BLI propulsor through a mechanical drivetrain. The STARC–ABL is predicted to provide a 3.4-percent reduction in fuel consumption relative to an advanced technology conventional aircraft for a single-aisle class, 3,500-nmi design mission and a 2.7-percent reduction for a 900-nmi economic mission. In comparison to the ST–ABL, the STARC–ABL provides a 2.5-percent reduction in fuel consumption for the design mission and 4.9-percent reduction for the economic mission. The STARC–ABL is also predicted to have a cumulative noise margin of 7 dB with respect to current noise limits. The ST–ABL has a cumulative noise margin of 5 dB. Areas for future research and evolution of the STARC–ABL concept include assessing its applicability to other aircraft sizes, increasing the fidelity of BLI and electric component modeling, and investigating the combination of an electrically driven fuselage BLI propulsor with other EAP architecture options.

1.0   Introduction

Electrified aircraft propulsion (EAP) has seen a tremendous increase in interest in the last 10 years. EAP encompasses a broad range of propulsion architectures, aircraft sizes, and types. The common feature of all of them is that electrical power is used to transmit some, or even all, of the propulsion energy. This distinguishes EAP from the more electrical aircraft (MEA) efforts where electrical power is used to replace hydraulic and pneumatic systems in the operation of nonpropulsion subsystems such as flaps, control surfaces, and landing gear actuation.

With electrical power as a common denominator, power from combustion engines, batteries, and fuel cells can be used together on the same EAP vehicle. An EAP system also allows power to be distributed

to a greater number of propulsors than is otherwise practical to achieve with independent turbofan or turboprop engines, and those propulsors to be put in places where an engine would not function well, such as in the boundary layer. Figure 1 illustrates the four cardinal types of EAP. Figure 2 illustrates how an EAP system can mix and match the basic elements in highly flexible architectures.

EAP systems are also not limited to a fixed mode of operation. One example investigated by Lents et al. (Ref. 1) is using electrical power only for takeoff and climb to better optimize the gas turbine engine design. The thrust lapse with altitude of a high bypass turbine engine is such that if the engine is sized to meet cruise thrust requirements with the core operating at the maximum continuous combustor exit temperature (Tt_4), the engine will likely not be able to meet the required takeoff thrust at the takeoff Tt_4. In a conventional system the only option would be to increase the size of the engine in order to meet the takeoff thrust requirement. This would result in a larger, heavier engine operating at a lower, less-efficient power setting during cruise. With an EAP system, a motor can be mounted on the fan shaft and energy from batteries, or another source of electrical power, can augment the power coming from the core to meet the takeoff thrust requirements. Power augmentation from the electric motor could then taper to a minimum at top of climb (TOC). During cruise, the engine would then be able to operate at its maximum continuous Tt_4 without power from the batteries. This allows the engine to operate with greater efficiency during cruise.
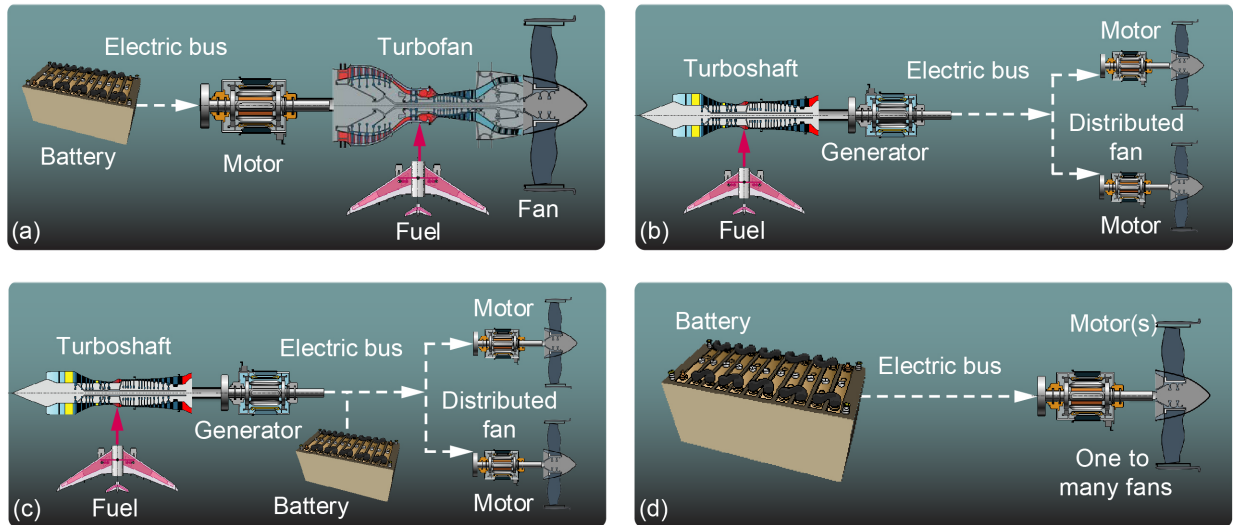

Figure 1.—Cardinal types of electrified aircraft propulsion systems. (a) Parallel hybrid. (b) Turboelectric. (c) Series hybrid. (d) All electric.
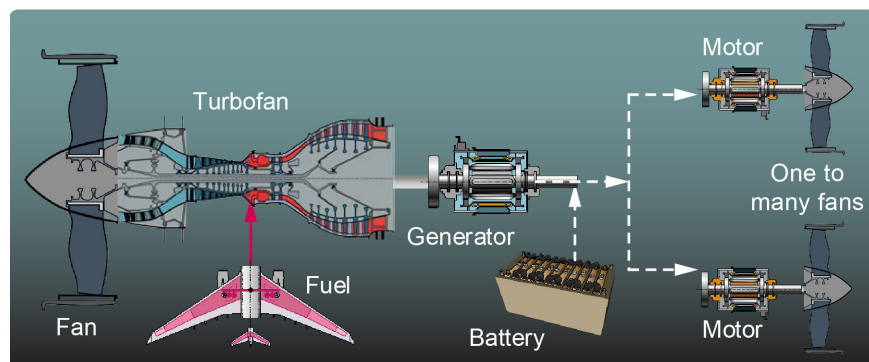

Figure 2.—High degree of flexibility in configuration of electrified aircraft propulsion systems.

EAP also greatly expands the design options for integrating and distributing propulsion by taking advantage of the flexibility to move electrical power across the vehicle in ways that would be difficult or impossible to do with shaft power. This enables engines to be placed where they can ingest clean, undisturbed air to maximize thermal efficiency, while propulsors can be placed to improve total system efficiency through synergistic propulsion-airframe integration (PAI). Some examples of synergistic PAI include the turboelectric N3–X (Ref. 2, Figure 3), where motordriven propulsors ingest a portion of the boundary layer while the turbogenerators on the wingtips ingest free-stream air; the hybrid-electric Parallel Electric-Gas Architecture With Synergistic Utilization Scheme (PEGASUS) (Ref. 3, Figure 4), where swirl from the wingtip propellers counteract the wingtip vortex, reducing induced drag; and the X–57 Maxwell (Ref. 4, Figure 5) where stowable propulsors on the leading edge of the wing increase the velocity over the wing during takeoff allowing the use of a smaller, more cruise efficient wing without an increase in takeoff speed compared to the same aircraft with a conventional wing.
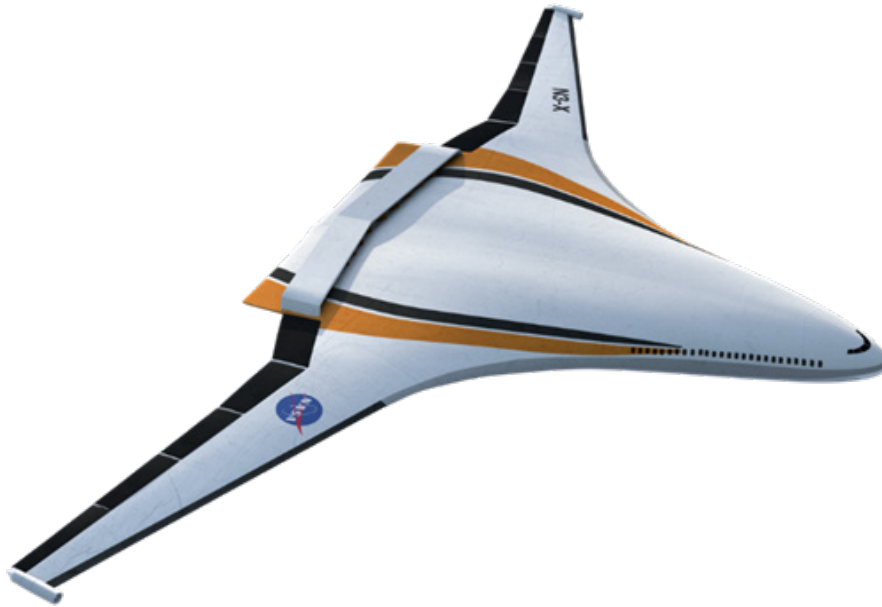

Figure 3.—Conceptual layout of turboelectric, hybrid wing-body N3–X concept.

Figure 4.—Hybrid-electric Parallel Electric-Gas Architecture With Synergistic Utilization Scheme (PEGASUS) concept.

Figure 5.—All-electric X–57 Maxwell.

EAP has potential environmental benefits that extended beyond the increases in efficiency enabled by more efficient propulsion and synergistic PAI. Hybrid-electric or all-electric systems can use electricity derived from low-emissions terrestrial power sources such as wind, solar, and/or nuclear power. The energy from these clean terrestrial power sources does not have to be stored in an onboard battery. For example, hydrogen that is produced from water and clean energy could be stored onboard and used to generate clean electricity with a fuel cell. Another important environmental consideration for air transport is noise. An all-electric aircraft eliminates combustion noise. However, since engine noise is only one portion of the total vehicle noise, a pure electric aircraft has the potential to be substantially quieter, but not completely silent. In vehicles that use combustion engines to drive generators as a source of electrical power, the flexibility of routing electrical power cables allows combustion engines to be positioned where the aircraft shields ground observers from engine noise while positioning propulsors in locations to best perform their functions (e.g., generate thrust, reduce drag, ingest the boundary layer, and/or augment lift).

The focus of this report is the use of an EAP system to power a propulsor that ingests the fuselage boundary layer. The fundamental efficiency benefit of BLI is illustrated in Figure 6. In a free-stream propulsor, the difference between free-stream and nozzle velocity is high while the velocity in the wake of the fuselage is slower than free stream. Both velocity differences represent losses in the overall vehicle system. By superimposing the propulsor and boundary layer streams, the velocity profile at the exit of the propulsor is much closer to the free-stream velocity. The result is that it is possible to require less power to yield the same net axial force for a BLI system than a conventional system.

A BLI configuration that ingests the fuselage boundary layer is especially appealing for a tube-and-wing configuration aircraft because the fuselage boundary layer represents a substantial portion of the boundary layer created by the aircraft and it can be captured by a single propulsor. Capturing the fuselage boundary layer has the added advantage that most of the velocity gradient in the boundary layer is in the radial or spanwise direction relative to the fan. As such, a given section of each fan blade does not see a significant variation in the relative inflow velocity as it rotates. This allows the velocity gradient in the boundary layer to be accommodated by setting the twist of the fan blades to the angle necessary to achieve the optimal angle of attack for each section along the length of the fan blade. Because the inflow velocity of the incoming air and the circumferential velocity of the fan are lowest at the hub and both increase along the span of the fan blades, the fans for ingesting the fuselage boundary layer will have less
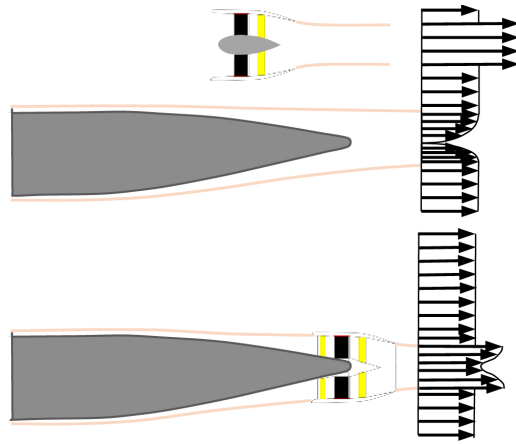
Figure 6.—Fuselage boundary layer ingestion.

twist than is required for fans where the inflow velocity is uniform from the hub to the tip of the fan. This simpler geometry will reduce the forces that are trying to untwist the fan blade during operation, and so it has the potential to reduce the weight of the fan for this application.

For a completely symmetrical tailcone without any flow disturbances at zero angle of attack, it is theoretically possible to design a fan blade that experiences no circumferential distortion, and thus, no efficiency penalty due to the velocity gradient in the boundary layer. In actual designs, the flow velocity coming into the propulsor is not circumferentially uniform due to downwash from the main wings, wakes from the vertical tail, and the need for tailcone upsweep to maintain adequate ground clearance during rotation at takeoff. This results in the fan experiencing some degree of circumferential distortion, which will decrease the fan efficiency. However, the amount of distortion is still much less than that experienced by propulsors embedded into the surface of aircraft like the NASA N3–X (Ref. 2) or the Massachusetts Institute of Technology D8 (Ref. 5). Studies by Ordaz et al. (Ref. 6) and Gray et al. (Ref. 7) have shown that small variations to the surface shape of the tailcone can substantially reduce the circumferential distortion induced by wing downwash and tailcone upsweep and so minimize the efficiency penalty.

The use of electrical power for propulsion does come with the cost of additional weight from the electrical system, losses in the electrical power system, and the weight and power of a thermal management system (TMS) to dissipate the resulting heat. Opportunities exist for reductions in weight in other parts of the propulsion system or aircraft that have the potential to offset some of the added weight from the electrical system and TMS. For example, for the same total flow area, multiple small fans weigh less than a single large fan. Thus, the net weight increase for an EAP system may be less than just adding the weight of the electrical system and TMS (Ref. 2). The electrical power losses and higher required thrust due to increased aircraft weight can significantly offset the efficiency gains from the synergistic PAI that is the reason for adding an EAP system.

However, a key advantage of turboelectric and hybrid electric approaches in distributed propulsion systems where the number of propulsors is greater than two is that the ability to distribute electric power over significant distances and for numerous individual propulsors allows all power to still be generated by two larger, generally more efficient core engines. This is especially advantageous for propulsion systems in which even with just two core engines the core flow rate is small enough that the overall pressure ratio (OPR), and thus the thermal efficiency of the core, is limited by the minimum compressor exit corrected flow rate (Wc_{3min}) rather than the maximum compressor exit temperature (Tt_{3max}).

In a conventional system, each propulsor is driven mechanically by its own core engine. The airflow into each core engine in a distributed propulsion system using conventional turbofan/turboprop engines is less than into the two core engines of an EAP-based distributed propulsion system. The result is that the OPR, and thus thermal efficiency at which Wc_{3min} is reached, is lower. Evaluation of the overall attractiveness of an EAP-based concept requires a thorough assessment of both the benefits and the penalties incurred with the EAP system in comparison to the benefits and penalties of a conventional system or a nonelectric distributed propulsion system.

2.0 Study Background

This report represents a comprehensive update of the original 2016 study of a 154-seat single-aisle turboelectric aircraft with aft boundary layer propulsion (STARC–ABL) (Ref. 8).

In the 2016 results, the fuel savings in comparison to an equivalent technology conventional configuration were predicted to be 6.8 percent for the 900-nmi economic range mission and 12.2 percent for the 3,500-nmi design mission. Published results for aircraft similar to the STARC–ABL show a substantially lower fuel consumption savings (Refs. 9–11). An in-depth review of the methodology used in the propulsion system model for the 2016 STARC–ABL study revealed an error in the inlet drag accounting. Once the force accounting was corrected, the predicted overall aircraft fuel savings for the STARC–ABL was similar, if still somewhat higher, than the other studies.

Bauhaus Luftfahrt has shown with their Propulsive Fuselage Aircraft Concept (Ref. 12) that EAP is not required to have a tailcone propulsor that ingests the fuselage boundary layer. The Bauhaus concept is for a 300-passenger, long-range aircraft. To quantify the impact of using an independent turbine engine to directly drive the BLI propulsor, a third aircraft, the single-aisle transport aircraft with aft boundary layer propulsion (ST–ABL), has been added to this study.

An estimate of the noise levels for the STARC–ABL and ST–ABL aircraft and how those noise levels compare to regulatory maximum has been added for this report.

The 2016 study was analyzed with a cruise Mach of 0.7, consistent with the single-aisle designs in the original Boeing Subsonic Ultra Green Aircraft Research (SUGAR) study (Ref. 13). The economic feasibility of reducing the cruise Mach number from ~0.8, consistent with current aircraft, to Mach 0.7 has since been questioned. As a result, advanced, single-aisle concept designs by Boeing and others have increased the cruise Mach number back to ~0.8 (Ref. 14). To reflect this change in industry outlook for the cruise speed of future aircraft, the cruise Mach number for this study was increased to 0.785, and the aircraft and propulsion system designs were updated accordingly.

2.1 N+3 Conventional Configuration (N3CC)

The N+3 conventional configuration (N3CC) is a 2035 technology level conventional tube-and-wing transport configuration that is used as the basis of comparison for the two fuselage BLI concepts studied in this report. The N3CC uses advanced technologies in both the airframe and propulsion systems that were assumed to be at technology readiness level (TRL) 6 by the year 2025, targeting an entry-into-service in the 2035 timeframe. The use of an advanced technology baseline is important so that the benefits of fuselage BLI and EAP technology can be isolated from other unrelated advanced technologies. The N3CC was originally based on characteristics of the Boeing Refined SUGAR concept using data from References 13–18. Key airframe technology assumptions include fuselage riblets for reduced viscous drag, advanced airfoils with laminar flow, a moderately high aspect ratio wing with the span constrained to 118 ft, advanced composite materials, and advanced air traffic management enabling optimized flight profiles. A complete list of aircraft technologies can be found in Reference 15. To

accommodate the higher cruise speed, the updated N3CC uses an advanced geared turbofan engine design based on the engine described in Reference 19. The key features of this engine are a fan pressure ratio of 1.3, a fan gearbox, and a variable area bypass nozzle.

The airframe and turbofan engines of the STARC–ABL and ST–ABL are based on the N3CC and differ only where required.

2.2 Single-Aisle Turboelectric Aircraft With Aft Boundary Layer Propulsion (STARC–ABL)

The STARC–ABL, illustrated in Figure 7, was conceived as a minimal EAP application for a tube and wing aircraft in which only a portion of the total propulsive power necessary to power the fuselage BLI propulsor is converted to electricity. In the STARC–ABL concept, approximately two-thirds of the propulsive power is still transmitted mechanically to the fans in the underwing turbofan engines. The STARC–ABL concept evolved from prior NASA investigations of the aerodynamic benefits of fuselage BLI (Ref. 20), NASA's prior exploration of turboelectric propulsion (Ref. 2), and the Boeing SUGAR Freeze concept (Ref. 21).

The BLI propulsor motor size of 3,500 hp and fan pressure of 1.25 selected in the initial 2016 STARC–ABL study (Ref. 8) were carried over to this study.

2.3 Single-Aisle Transport Aircraft With Aft Boundary Layer Propulsion (ST–ABL)

The ST–ABL, illustrated in Figure 8, has a BLI propulsor at the tip of the fuselage tailcone identical to the STARC–ABL. However, in place of the EAP system of the STARC–ABL, an independent turboshaft engine mounted in the vertical tail drives the BLI propulsor using mechanical shafting. ST–ABL has been included in this report to quantify the difference in fuel consumption between the STARC–ABL and an aircraft that has three smaller core engines but does not have the losses and weight of the STARC–ABL electrical transmission system.

Figure 7.—Artist conception of single-aisle turboelectric aircraft with aft boundary layer propulsion (STARC–ABL) showing integration of boundary layer ingestion propulsor and T-tail.
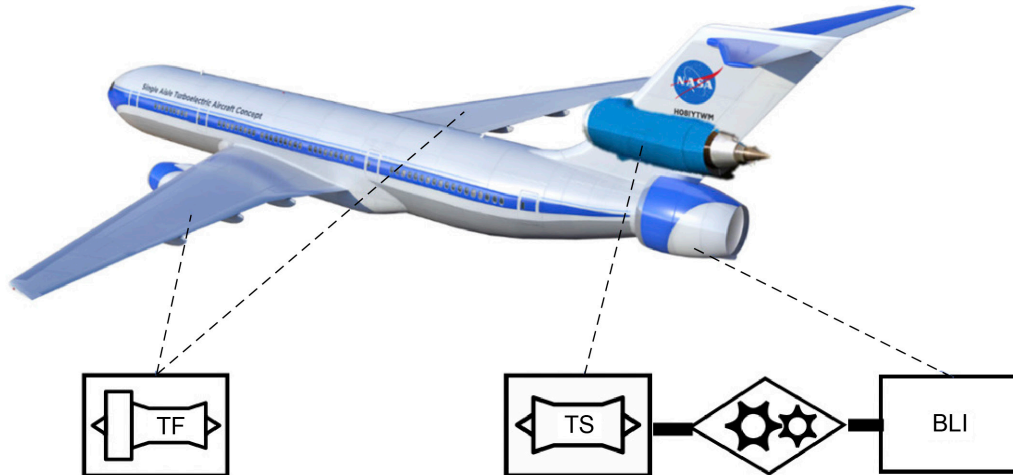
Figure 8.—Single-aisle transport aircraft with aft boundary layer propulsion (ST–ABL) system architecture. Turbofan (TF). Turboshaft (TS). Boundary layer ingestion (BLI).

The propulsion system aerodynamic design point (ADP) flight condition selected is the optimal TOC for each aircraft. The turboshaft engine driving the BLI propulsor in the ST–ABL is sized to provide the same 3,500 hp to the BLI propulsor at the ADP as the STARC–ABL electrical power system. However, the turboshaft running at its maximum turbine inlet temperature at the rolling-takeoff (RTO) point produces substantially more power. As a result, the BLI propulsor in the ST–ABL produces much greater thrust at RTO than the STARC–ABL, which is limited to the 3,500 hp output of the electric motor regardless of altitude or speed. The ST–ABL has two turbofan engines under the wings that have an identical configuration and technology level as the N3CC turbofans, but which are smaller since the tail-mounted turboshaft and BLI propulsor provide a significant portion of the total aircraft thrust.

2.4   Design and Economic Range Missions

The design mission for all three aircraft is 3,500 nmi carrying 30,800 lb of payload at a fixed cruise Mach of 0.785 and optimum cruise altitude to maximize specific range. Although the aircraft were required to fly the 3,500-nmi design mission, the designs were optimized using the sum of the fuel consumption for the design mission and a 900-nmi economic mission as the objective. The propulsion system was required to have sufficient thrust to meet the minimum second segment climb and missed approach gradients in the event of a single engine failure. The propulsion system must also produce sufficient thrust to meet the initial cruise altitude capability requirement of being able to climb at 300 ft/min at the optimal starting cruise altitude. The optimal TOC and start of cruise altitude with the engine operating at the maximum continuous power setting was used as the ADP for each aircraft. The maximum allowable takeoff and landing field lengths are 8,190 ft, and the approach velocity was limited to 150 kn.

The mission profile used for all three aircraft, shown in Figure 9, is based on the profile used in Reference 11.
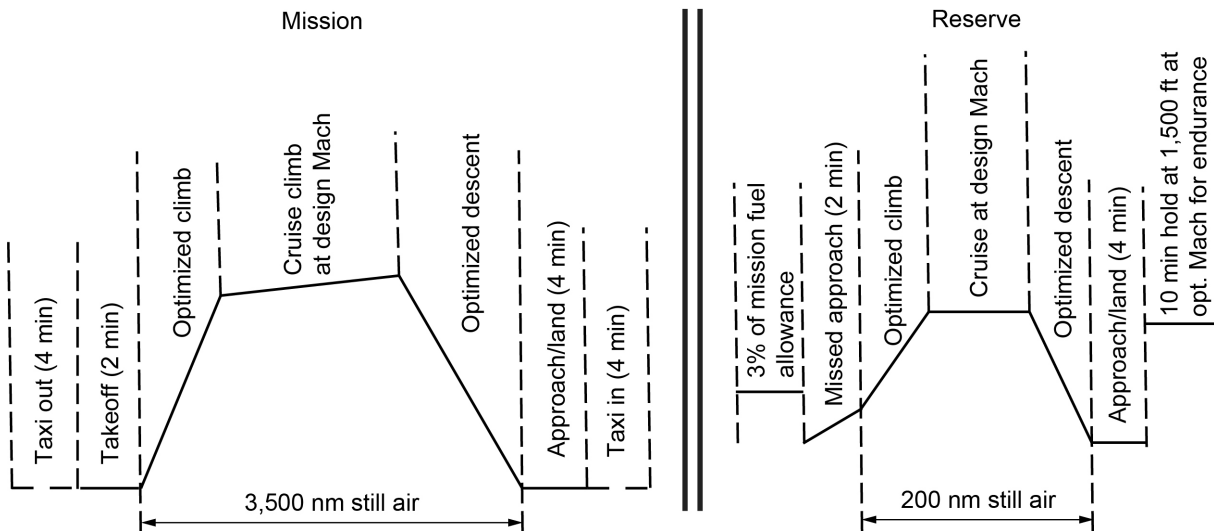
Figure 9.—Common design mission profile.

3.0 Analysis Methodology

The unconventional nature of the EAP system and BLI propulsor necessitated several enhancements or modifications to existing analysis tools. The methodology used for modeling and analyzing the propulsion system performance, propulsion weight, aircraft sizing and performance, and noise characteristics are in the following sections.

3.1 Propulsion System Performance Modeling

Cycle analysis for the propulsion systems was performed with the Numerical Propulsion System Simulation (NPSS) code (Refs. 22 and 23). All three propulsion systems were designed with the same technology assumptions for turbomachinery efficiency, temperature limits, and corrected flow limits.

Thrust values required by the aircraft at the ADP and RTO conditions, the turbofan extraction ratio (the ratio between the core and bypass nozzles exit total pressures) at the midcruise condition, and the two high-pressure turbine (HPT) cooling flows at the RTO are specified. To yield a propulsion system design that meets the specified performance at all flight conditions, a multidesign point (MDP) structure was created in the NPSS models of the propulsion systems for each vehicle.

In this structure, the ADP (running in design mode) and the RTO and midcruise cases (running in off-design mode) are put inside an outer iteration loop controlled by a separate solver, termed here as the MDP solver. The MDP solver iterates the outer loop around the ADP, RTO, and midcruise points. For each iteration, the MDP solver varies the values of selected parameters used as input in the ADP case until the values of an equal number of selected output variables in the RTO and midcruise cases are equal to specified values. For all three propulsion systems in this report, the MDP solver varies the turbofan inlet airflow and bypass ratio, as well as the two turbine cooling flows at the ADP, until either the ADP thrust target or the RTO thrust target, depending on which one is more limiting; the extraction ratio at midcruise; and the required turbine cooling flow at the RTO are met.

In conventional propulsion systems where the individual engines are identical, it is normal for the performance of the propulsion system to be represented by the performance of a single engine. For the STARC–ABL and ST–ABL aircraft, this is not the case. As a result, the entire propulsion system has to be treated as a single unit. Thus, for these systems, the thrust given is the total system thrust, unless specifically identified, and represents the sum of the thrusts of all elements of the system. The fuel flow is

the total system fuel flow and is the sum of the fuel flows of all turbine engines in the system. The thrust-specific fuel consumption (TSFC) is the total system fuel flow divided by the total system thrust. Lastly, the effective bypass ratio is the total flow of all fan air not going through a turbine core engine divided by the total of the air going through all of the turbine core engines. This total system approach is also used for the N3CC to give a common basis for comparison, even though the two turbofan engines are identical and the performance of just a single turbofan would be sufficient to represent the performance of the entire propulsion system.

3.1.1   N+3 Conventional Configuration (N3CC)

The two underwing turbofans of the N3CC are based on an advanced technology turbofan engine, which is meant to represent the expected capabilities of gas turbine engines entering service in the 2030 to 2040 timeframe. The engine is a conventional two-spool, separate flow gas turbine engine with application of technology improvements to reduce fuel consumption. Details on the technology assumptions for this engine can be found in Reference 19. The allowable lower limit on the core flow size parameter, Wc_{3min}, was set to 2.5 lbm/s for the N3CC engine. The thrust required for the N3CC is about 25 percent less than that provided by the engine designed in Reference 19. Both engines are limited by the Wc_3. The lower design thrust for the N3CC turbofan results in a reduced core inlet flow rate, which in turn limits the N3CC turbofan to an OPR of 47, while the larger engine in Reference 19 has an OPR of 55. The N3CC turbofans were sized for a fan pressure ratio of 1.30 with a gear ratio of 2.8. The engine layout for estimating performance and weights is shown in Figure 10.

3.1.2   Single-Aisle Turboelectric Aircraft With Aft Boundary Layer Propulsion (STARC–ABL)

A schematic of the STARC–ABL propulsion system architecture is shown in Figure 11. For STARC–ABL, the propulsion system consists of two underwing turbofans and an electric system that drives the fuselage BLI propulsor. A generator is mounted on the high-speed side of the gearbox in each underwing turbofan. They are sized to deliver 3,500 hp in shaft power to the BLI propulsor. The underwing and BLI propulsor fans are sized for fan pressure ratios of 1.30 and 1.25, respectively. The gear ratio for the underwing engines is 2.7 and for the BLI propulsor is 3.0. The engine layouts for estimating performance and weights of the STARC–ABL propulsion system are shown in Figure 12.
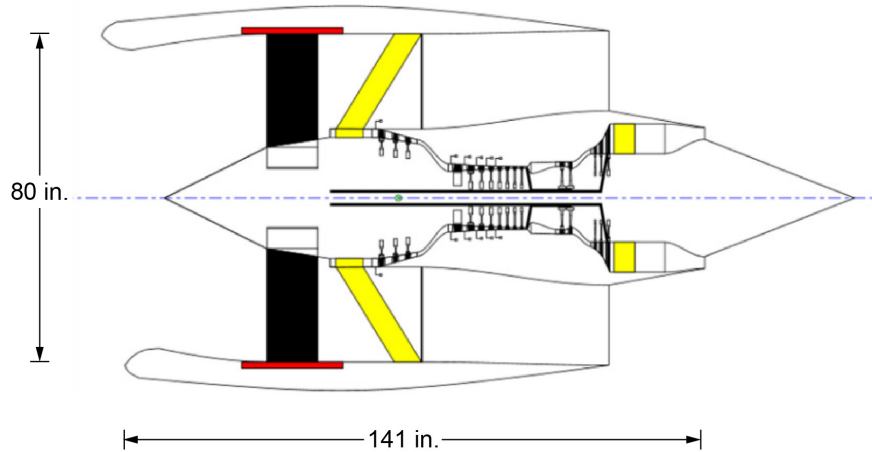
Figure 10.—N+3 conventional configuration (N3CC) propulsion system.
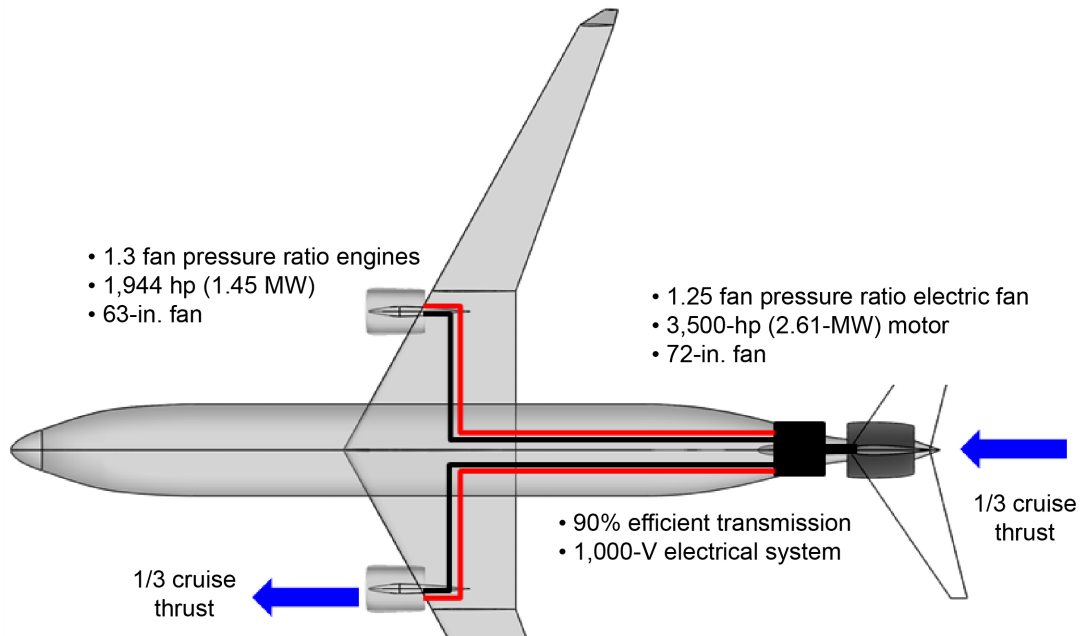
Figure 11.—Single-aisle turboelectric aircraft with aft boundary layer propulsion (STARC–ABL) system architecture.
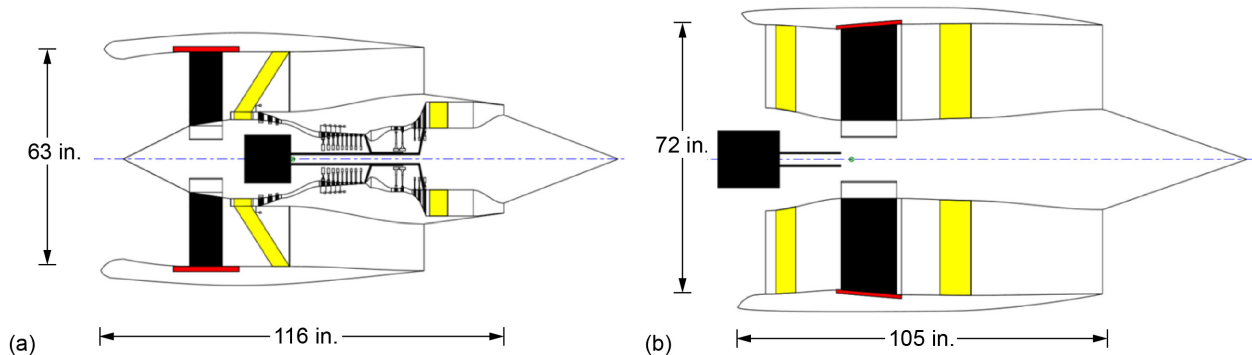
Figure 12.—Layout of single-aisle turboelectric aircraft with aft boundary layer propulsion (STARC–ABL) system. (a) Underwing turbofan. (b) Tailcone propulsor.

3.1.2.1 Turbofan Engines

The turbofan engines for the STARC–ABL are derivatives of the engines used on the N3CC. The major modification is the insertion of a generator on the high-speed side of the fan gearbox. Because the maximum motor power to the BLI propulsor is constant regardless of altitude or speed, the BLI propulsor fan is only able to spin at around 65 percent corrected speed at the RTO. Thus, the BLI propulsor contributes only about 14 percent of the total thrust at the RTO, whereas it contributes 35 percent at the ADP. As a result, the fan on the underwing turbofan will spin faster because the generator is taking a much lower fraction of the turbine power at the RTO than it is at the ADP. If the ADP turbofan fan speed is simply set to 100 percent corrected speed, the fan speed at the RTO is too fast. Therefore, an extra independent/dependent pair was added to the MDP method for the STARC–ABL system that varies turbofan fan percent corrected speed at the ADP until the fan corrected speed at the RTO is at a maximum allowed value (in this case, 105 percent corrected speed was used).

3.1.2.2 Boundary Layer Ingestion Propulsor

The BLI propulsor is a highly coupled system with interactions between the airflow over the aircraft fuselage, especially the tailcone, and the internal aerodynamics of the propulsor that need to be captured to estimate the performance of this key subsystem.

The 2016 results used the boundary layer profile calculated for a clean (no BLI propulsor) symmetrical tailcone (Ref. 17). The BLI propulsor was superimposed onto this flow field and the mass averaged velocity, density, and total pressure profiles for this clean tailcone flow at the axial location of the inlet of the BLI propulsor were assumed to represent the average fluid properties going into the BLI propulsor. The presence of the BLI propulsor had no effect on the flow field upstream of the inlet. This is what is now called an uncoupled analysis. In this 2016 analysis, the increasing static pressure of the diffusing flow over the tailcone was overlooked, and hence, the static pressure drag (the difference between the integrated static pressure over the inlet area and the integrated static pressure field over the area of the nozzle) was not included in the inlet drag. This is what caused the estimated fuel savings in the initial reporting of the STARC–ABL to be much larger than it should have been.

The BLI propulsor model in NPSS for this analysis of the STARC–ABL (and ST–ABL as well) was based on the concept of the power savings coefficient (PSC), which is a BLI figure of merit first introduced by Smith (Ref. 24). The PSC reduces the complex interactions of the BLI propulsor into a single number comparing the power required for the BLI configuration (P_{BLI}) to that of a reference, non-BLI configuration ($P_{\text{free-flier}}$) with the same net force:

$$PSC = \frac{P_{\text{free-flier}} - P_{BLI}}{P_{\text{free-flier}}}$$

(1)

Gray (Ref. 25) estimated the PSC metric for a fuselage-only version of the STARC–ABL with a symmetrical tailcone using 2-D computational fluid dynamics (CFD) models. The BLI model placed the BLI propulsor on the tailcone and evaluated both the external flow as well as the flow inside the BLI propulsor with an actuator disk representing energy addition from the fan. For a given shaft power input into the BLI fan (P_{BLI}), the net axial force (summation of all external and internal forces in the axial direction) was calculated. The non-BLI CFD model had a fuselage and clean tailcone with a "free-flier" propulsor. The free-flier propulsor had a free-stream inlet but without any structural connection to the fuselage. The free-flier propulsor model also used an actuator disk with the same pressure ratio as the BLI propulsor and a given amount of shaft power ($P_{\text{free-flier}}$) to the actuator disk. As with the BLI model, the axial forces from both the fuselage and the separate propulsor were totaled. The $P_{\text{free-flier}}$ was varied until the net axial force in the free-flier model was the same as the BLI model. With the two power levels known, Equation (1) yields the value of the PSC for the given BLI propulsor.

Gray's work (Ref. 25) shows it is critical to address the full vehicle, both external and internal aerodynamics, as a unified problem. This was corroborated by the analysis of Ahuja and Mavris (Ref. 26). Simply using the mass-averaged velocity and area-averaged static pressure derived from the clean flow-field boundary layer with the BLI propulsor superimposed on it gives approximately half of the benefit from BLI than does solving the problem as a single, coupled problem as in Reference 25. Figure 13 illustrates this difference. The results of Gray's work form the basis for the PSC values used in the NPSS model for this study.
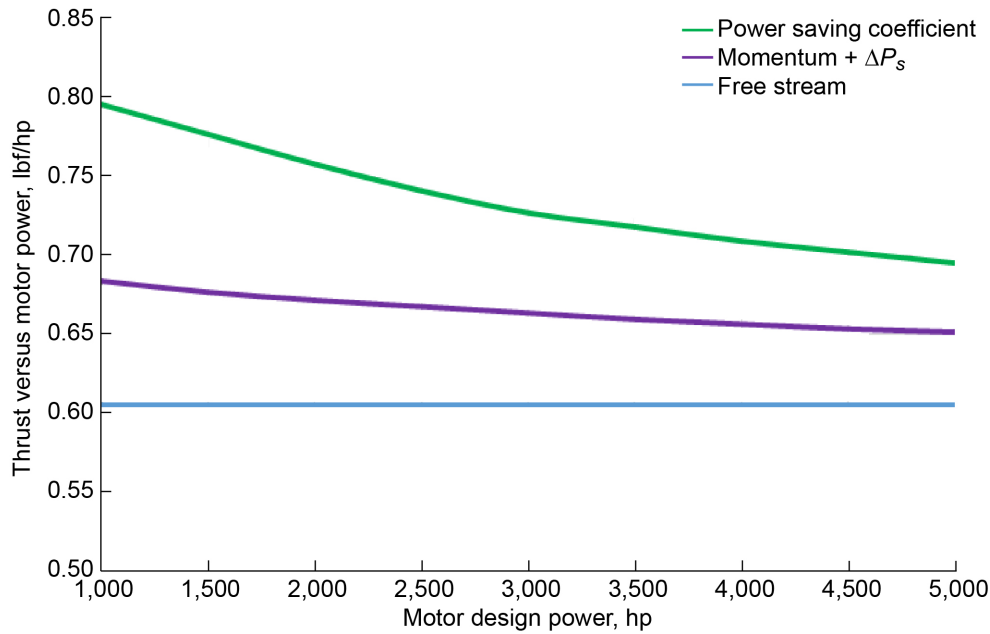
Figure 13.—Comparison of boundary layer ingestion (BLI) impacts using power savings coefficient from coupled analysis versus decoupled superposition of propulsor and fuselage boundary layer. The "Momentum + ΔP_s" line represents the decoupled method where the inlet drag is determined by the mass average momentum and area-averaged static pressure of the flow from the clean tailcone flow field at the axial location of the BLI propulsor inlet.

The motor power driving the BLI propulsor (P_{BLI}) is a given, and the *PSC* for the STARC–ABL at that power level was calculated by Gray. Solving Equation (1) for $P_{\text{free-flier}}$ yields

$$P_{\text{free-flier}} = \frac{P_{BLI}}{1 - PSC} \tag{2}$$

Using the *PSC* in this way, the propulsion system model does not need to contain a representation of the boundary layer flow in order to calculate the thrust of the BLI propulsor. Instead, it only needs the free-stream flow conditions, the BLI motor power, and the *PSC*. Equation (2) gives the motor power of the free-flier ($P_{\text{free-flier}}$) that will yield the same net axial force (propulsor thrust – fuselage drag), when driving the free-flier propulsor with free-stream inlet conditions, as for the actual BLI propulsor with boundary layer inlet conditions when driven with the actual motor power (P_{BLI}). It should be noted that with this *PSC* approach there is no drag benefit attributed to the fuselage from the BLI. The entire BLI benefit, whether considered reduction in fuselage drag or increase in propulsive efficiency, is encompassed in the *PSC* value.

In this study, only a single *PSC* value was available. It was assumed that at low speeds the *PSC* was small. Thus, for velocities up to Mach 0.3, the *PSC* was assumed to be zero. Above Mach 0.6, the given *PSC* was used, and a linear interpolation was made for velocities between. Since the majority of the total mission energy is consumed during cruise, this should represent a reasonable approximation of the results of the more complete case where the *PSC* is available for a range of altitudes, speeds, and motor power levels.

The *PSC* method that uses the thrust of the free-flier propulsor driven by $P_{\text{free-flier}}$ to represent the thrust of the BLI propulsor does not provide the correct airflow, pressure, temperature, or shaft speeds to allow the weight and flow path of the BLI propulsor to be determined. To determine the actual flow rates,

pressures, and temperatures, a second propulsor model representing the actual BLI propulsor was added to the system model. This second propulsor uses the actual power of the BLI propulsor (P_{BLI}) and the boundary layer profile to determine the inlet mass-averaged velocity, total pressure, total temperature, and area-averaged static pressure, providing the information necessary to determine the actual flow path and weight of the BLI propulsor. However, the thrust calculated by the BLI propulsor model is not used since it does not contain all of the forces internal and external to the BLI propulsor that are accounted for in the *PSC* method.

As a symmetrical cone, the boundary layer flow field used in this analysis does not have the circumferential variation that would come from downwash from the main wings and a tailcone with upsweep to accommodate ground clearance. The necessary CFD analysis has been done by Ordaz (Ref. 6). Future analysis should use these results to calculate updated *PSC* values for the BLI propulsor model. Also, the flow field over the realistic tailcone with the BLI propulsor in place will be needed to predict the "installed" flow rate, temperature, and pressures at the BLI propulsor inlet in order to update the weight and size estimates.

3.1.2.3 Electrical System

The electrical system for the STARC–ABL propulsion system consists of a generator located on the turbine side of the gearbox of the fan shaft for each underwing turbofan engine. The alternating current (AC) power created by the generator is then converted to direct current (DC) by an active rectifier. The DC power is carried along electrical cabling to the tailcone of the aircraft and transmitted to the motor driving the BLI propulsor fan, where it is converted from DC back to AC by an inverter and used to drive a single 3,500 hp variable frequency AC motor. The AC to DC to AC conversion process allows the speed of the shaft driving the generator to be independent of the shaft speed of the BLI propulsor. Without the DC link, the frequency, and thus shaft speed, of the BLI propulsor motor would have to stay within a very narrow fixed ratio of the shaft speed of the generators.

The motor, generators, and power electronics in the electrical system were modeled with simple specific power assumptions and constant efficiencies. Motor and generator performance maps would provide a better estimate of efficiency at off-design speed and torque values. However, most motors and generators operate at nearly constant efficiency over a broad range of torque and speeds around the motor design point. The motor and generators in the STARC–ABL system are operating at, or very close to, the design speed and torque at the key operating conditions of takeoff, climb, and cruise, where nearly all fuel is consumed. Thus, using a constant efficiency will yield sufficiently accurate results for this phase of analysis.

Table 1 contains the assumed specific powers and efficiencies for each of the major components in the STARC–ABL electrical system. Most of these values were based on research goals established by the Advanced Air Transport Technology (AATT) project in NASA. The rectifier and inverter efficiency assumptions reflect recent advancements in power converter technology (Ref. 27).

TABLE 1.—ELECTRICAL COMPONENT ASSUMPTIONS

Component	Specific power, hp/lb (kW/kg)	Efficiency, percent
Generator	8.0 (13.2)	96
Motor	8.0 (13.2)	96
Rectifier	11.6 (19.1)	99
Inverter	11.6 (19.1)	99

The system voltage was assumed to be 1,000 V. Aircraft electrical systems do not currently exceed 270 V to provide sufficient margin to avoid exceeding 327 V, the minimum voltage required to initiate an arc across an airgap as defined by the Paschen equation (Ref. 28). Using a floating ground allows voltage to go between –270 and +270 V for a total voltage of 540 V. However, even at 540 V transmitting 1.38 MW requires each cable from the generator to the motor to carry 2,500 A. This large current level will require a large diameter cable and result in high electrical system weights. For this reason, a system voltage of 1,000 V was assumed for this study.

Voltages above 540 V require that charge never be allowed to leak out of the cable and charge the rest of the aircraft. This will require additional development of high-voltage cables that can operate safely in aircraft. The selected 1,000 V system is not an optimum value. Voltages higher than 1,000 V would result in further reductions in the electrical system weight and should be explored in future analysis.

3.1.2.4 Thermal Management System

The TMS in the NPSS model represents just the cooling system required by the electrical power system consisting of the generators, rectifiers, cables, inverter, and motor. The High-efficiency Electric Aircraft Thermal Research (HEATheR) effort at NASA (Ref. 29) conducted a very detailed analysis of the TMS of the STARC–ABL. In that study, a TMS weighing 241 lb was designed that was capable of dissipating 554 hp of heat using heat pipes to transport heat to panels on the aircraft where forced convection of the airflow over these panels was sufficient to reject the heat to the atmosphere without the need for drag-producing radiators. This results in a weight factor of 2.3 hp/lb.

3.1.3 Single-Aisle Transport Aircraft With Aft Boundary Layer Propulsion (ST–ABL)

In order to conduct a fair comparison between the turboelectric and mechanically driven BLI architectures, some parameters were held constant between STARC–ABL and ST–ABL, such as the fan pressure ratios and component efficiencies. The BLI propulsor design was the same for both concepts, using the *PSC* approach described in Section 3.1.2.2. To maintain similarity with STARC–ABL, the turboshaft engine was sized to produce 3,500 hp at TOC, and the underwing turbofans were sized to provide the remainder of the total thrust. This results in a core engine size for the underwing turbofan engines that is considerably smaller than the STARC–ABL turbofan engines because they do not need to produce power for the BLI propulsor. Unlike the electric motor and generators in the STARC–ABL, which have the same maximum power at all altitudes, the shaft power available from the turboshaft engine of the ST–ABL to drive the BLI propulsor increases as the altitude decreases.

The engine architecture of the ST–ABL underwing turbofans is the same as the N3CC. As with the N3CC and STARC–ABL, the OPR is limited by the minimum compressor exit corrected flow rate of 2.5 lbm/s. The turboshaft engine has a two-spool configuration with a single multistage compressor driven by a HPT and an independent power turbine connected to a gearbox powering the BLI propulsor. The underwing and the BLI propulsor fans are sized for the fan pressure ratios of 1.30 and 1.25, respectively. The gear ratio for the underwing engine is 2.6 and for the BLI propulsor is 3.1. The engine layouts for estimating performance and weights of the ST–ABL propulsion system are shown in Figure 14.
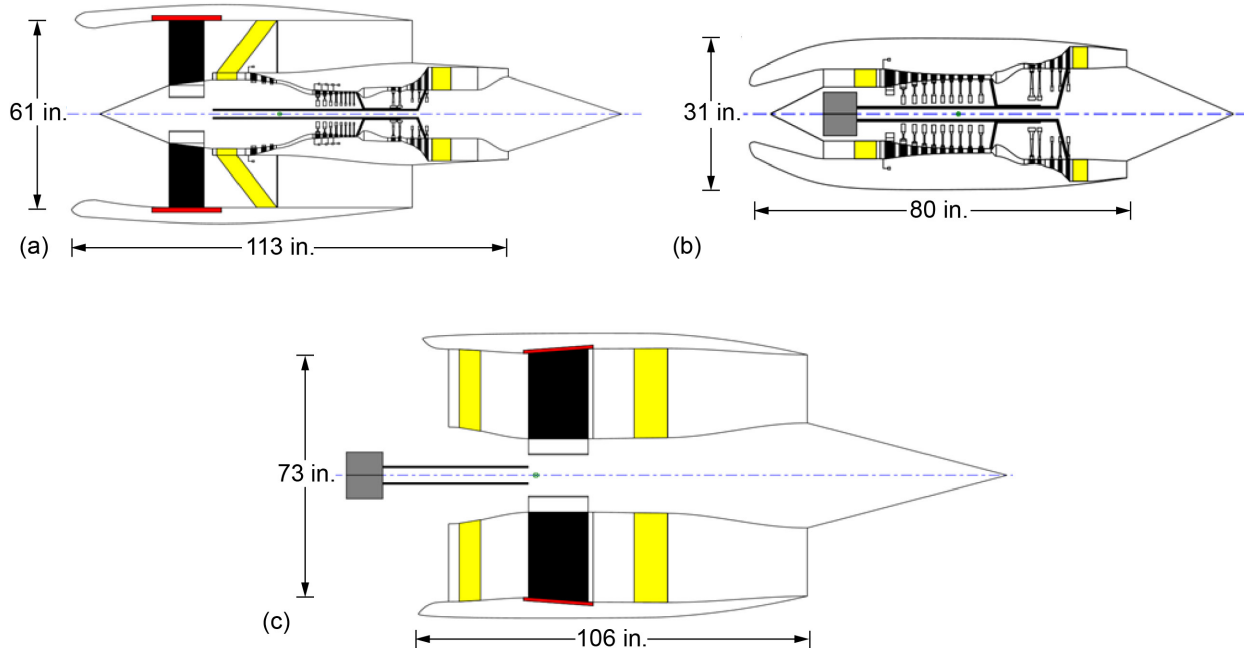
Figure 14.—Layout of single-aisle transport aircraft with aft boundary layer propulsion (ST–ABL) system. (a) Underwing turbofan. (b) Turboshaft engine. (c) Tailcone propulsor.

3.2   Propulsion System Weight Modeling

Following the engine cycle model development, estimates of the weights and flow path dimensions were developed for the N3CC, ST–ABL, and STARC–ABL propulsion systems. The NASA software tool, Weight Analysis of Turbine Engines (WATE++) (Ref. 30), was used to create engine architectures that could achieve the engine thermodynamic cycles produced by the NPSS models detailed in the previous sections. The cycle data required for WATE++ execution, such as air mass flow, temperatures, pressures, pressure ratios, etc., were derived from the NPSS cycle model output. Both the ADP and off-design cases were used to encompass the maximum performance level (i.e., temperature and pressure) required to size each engine component. The cycle data, material properties, and design rules for geometric, stress, and turbomachinery stage-loading limits were used to determine an acceptable engine flow path.

For the turbofan and turboshaft engines, the turbine stator vane materials were assumed to be high-temperature (i.e., third generation) ceramic matrix composites. Nickel-based alloys were assumed for the turbine rotor blades, with the exception of the last stage of the low-pressure turbine (LPT) for which titanium aluminide was assumed. A NASA-developed empirical correlation (Ref. 31) was used to calculate the gearbox and lubrication system weights required as part of the low-pressure shaft. The correlation is a function of the maximum delivered output power, the shaft speed of the engine shaft coming into the gearbox, the shaft speed of the rotor or propeller shaft coming out of the gearbox, and a multiplier "K" that is varied to represent different technology levels. It was developed based on data from over 50 rotorcraft, tilt rotor, and turboprop aircraft. This correlation is shown in Figure 15 where "hp" is the power delivered to the fan in horsepower and "rpm" is the input and output shaft speeds in revolutions per minute. A K value of 72 representing future technology was used for the current assessment.
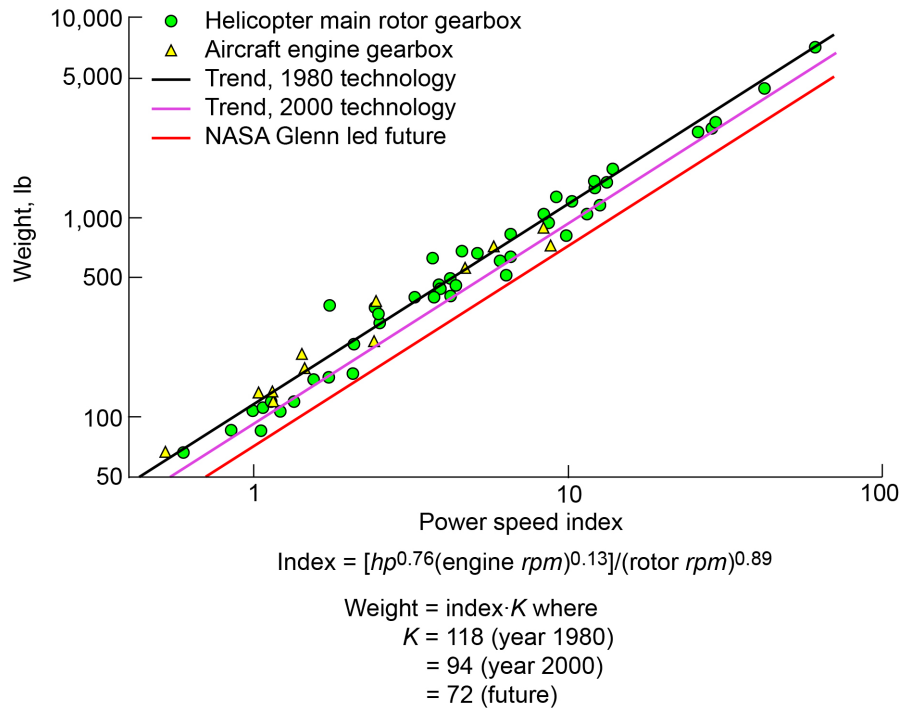
Figure 15.—Transmission and lubrication system weight correlation. Horsepower (*hp*). Revolutions per minute (*rpm*). Technology factor (*K*).

Below the figure, the equations shown are:

$$\text{Index} = [hp^{0.76}(\text{engine } rpm)^{0.13}]/(\text{rotor } rpm)^{0.89}$$

Weight = index·*K* where
K = 118 (year 1980)
   = 94 (year 2000)
   = 72 (future)

Weight estimates for the STARC–ABL electrical power system and TMS are based on the methodology and assumptions discussed in Section 3.1.2.4.

3.3 Aircraft Sizing and Mission Analysis

The aircraft system models were created using a variety of conceptual design tools to size the vehicles and determine mission performance. The sizing and analysis process is shown in the flowchart in Figure 16. First, design variables such as wing area and maximum thrust are chosen, indirectly setting wing and thrust loading for the aircraft. Next, a series of scripts determine dimensions for the wing and empennage, sizing the vertical and horizontal stabilizers using a simple volume coefficient metric and an engine-out trim constraint based on the vertical tail's effectiveness in countering yawing moments created by an engine-out condition during takeoff. Tail size is iterated until a size that meets all constraints is found. Open Vehicle Sketch Pad (OpenVSP) (Ref. 32) is used to model the outer mold line of the aircraft based on the dimensions previously calculated. Detailed geometry information and wetted area calculations are the outputs of the OpenVSP model that are provided to the Flight Optimization System (FLOPS) (Ref. 33), a conceptual aircraft design sizing and synthesis tool.

The propulsion system model is also an input to the FLOPS model in the form of a single table of propulsion system performance data, referred to as an "engine deck," along with propulsion system weight. A 5-percent installation penalty was added to overall propulsion system weight. Even though STARC–ABL and ST–ABL have two distinct propulsor types (underwing and fuselage BLI), the combining of propulsion system performance into a single table is necessary because FLOPS can only accommodate a single type of engine. This results in some compromise in the design as the BLI fan must use a predetermined power schedule and cannot be throttled independently from the underwing engines. This also impacts how performance requirements such as one-engine-inoperative (OEI) climb gradient are

assessed in the FLOPS analysis. The STARC–ABL and ST–ABL aircraft are modeled as two-engine aircraft in FLOPS. In an OEI condition, available thrust is half the all-engines-operating value. This may be approximately true for STARC–ABL where the loss of one underwing engine would also reduce the power available to the BLI propulsor. However, for ST–ABL, the loss of an underwing engine would not impact the thrust from the BLI propulsor. Because FLOPS is not aware of the BLI propulsor as an independent, separate engine, OEI performance for takeoff is calculated with a smaller thrust than is actually available, which may result in a longer takeoff field length.

Performance constraints were applied based on certification requirements for two-engine aircraft. It is not obvious whether future regulators would classify these vehicles as three-engine or two-engine aircraft, but a two-engine classification was assumed since the BLI propulsor on STARC–ABL is dependent on the underwing engines. The FLOPS model is used to size the aircraft to the design mission, computing weights, aerodynamic tables, takeoff and landing field lengths, and overall mission performance metrics.
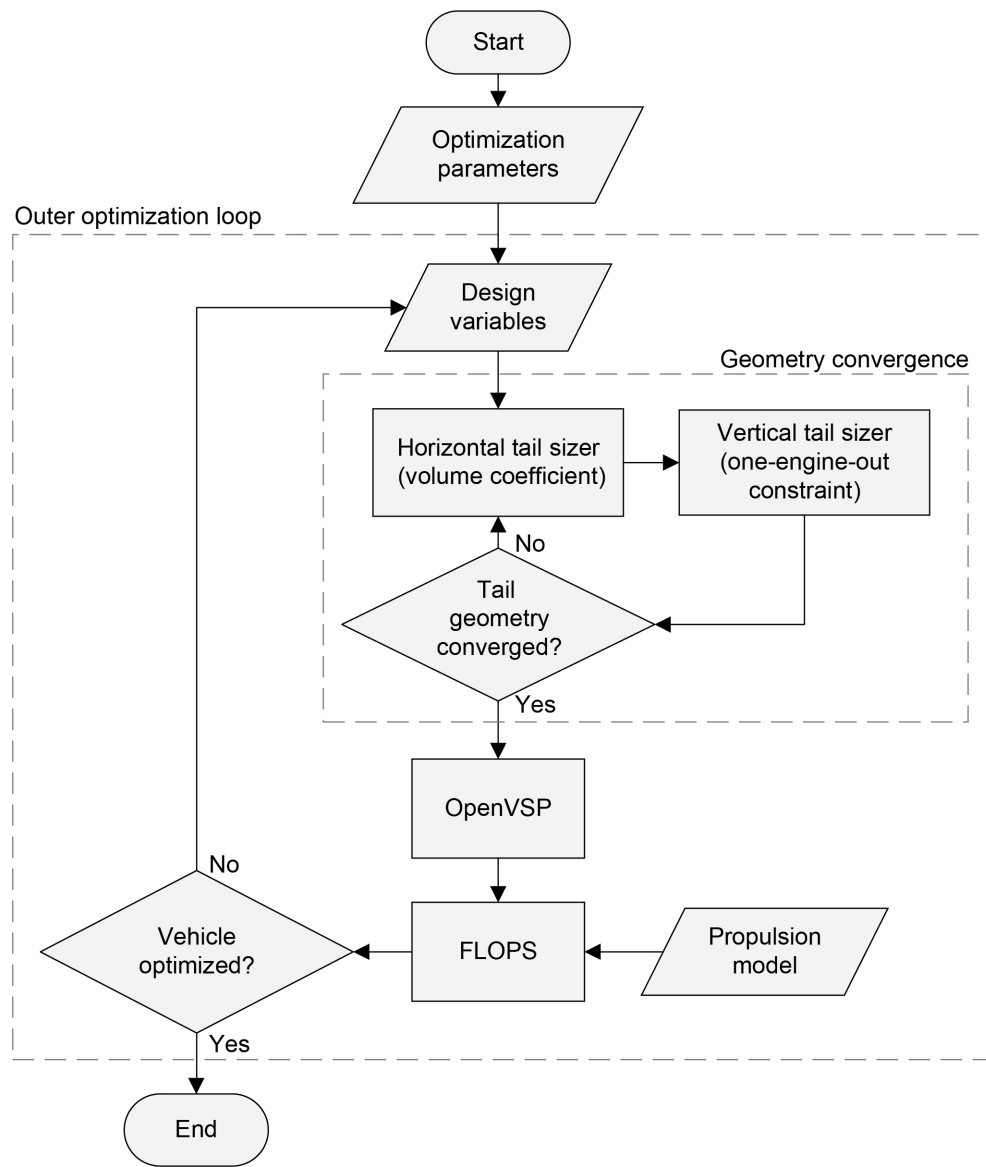

Figure 16.—Aircraft sizing process. Open Vehicle Sketch Pad (OpenVSP). Flight Optimization System (FLOPS).

TABLE 2.—CONSTRAINTS IN AIRCRAFT SIZING

Metric	Constraint
Takeoff field length, ft (m)	<8,190 (2,496)
Landing field length, ft (m)	<8,190 (2,496)
Approach velocity, kn (km/h)	<150 (241)
Time to climb, min	<30
Specific excess power, top of climb, ft/min (m/min)	>300 (91.4)

This entire model was wrapped with an external optimizer to select the thrust and wing loading that minimizes a weighted sum of the fuel consumption for the 3,500-nmi design mission and the 900-nmi economic mission. The optimization was constrained by operational performance restrictions as shown in Table 2.

ST–ABL was modeled using the STARC–ABL model as a starting point with slight modifications. An additional nacelle representing the turboshaft engine was mounted in the vertical stabilizer similar to trijet configurations. This nacelle was included in the OpenVSP model, which provided wetted areas for FLOPS. The ST–ABL propulsion system was incorporated into FLOPS in the same manner as STARC–ABL with a single combined engine deck. The same design mission and optimization constraints used to size STARC–ABL were also used to size ST–ABL.

3.4 Noise Analysis

Certification noise is estimated using standards and recommended practices defined by Annex 16 noise regulations (Ref. 34). All noise predictions are made with the NASA Aircraft Noise Prediction Program (ANOPP) (Refs. 35 and 36) using methods currently available within the code.

For the underwing turbofan engines, jet noise is predicted using a method developed for coannular jets by Stone et al. (Ref. 37). Fan noise is predicted using a method developed for high bypass ratio fans by Kontos, Janardan, and Gliebe (Ref. 38). Engine core noise is predicted by a method developed by Emmerling, Kazin, and Matta (Ref. 39). Liner treatment performance is estimated by a method given by Kontos, Kraft, and Gliebe (Ref. 40). Propulsion-airframe interactions are modeled using a wing reflection method available within ANOPP. For all propulsion noise methods, engine state data computed by NPSS are fed into ANOPP as functions of airspeed, altitude, and engine power setting. Landing gear noise is predicted using the Boeing airframe method of Guo (Ref. 41). Flap, slat, and trailing edge airframe sources are predicted using the Fink method (Ref. 42).

For the aft propulsor, treated fan noise is predicted using the Kontos methods as previously mentioned, but with special adjustments to account for inflow distortion influences due to BLI. The vertical tail, wing downwash, and fuselage upsweep contribute to distortion of the aft propulsor inflow. But detailed CFD analyses have shown that circumferential distortion can be mitigated by tailoring the shape of aft surfaces (Refs. 6 and 7). Also, flow entering the propulsor inlet is diffused and made more uniform by the front frame of the propulsor such that circumferential "one-per-rev" distortion from the vertical tail structure should be minimized. Thus, distortion is assumed to be radially dependent only and symmetric about the propulsor axis. Radially dependent distortion is accounted for with "adder" penalties applied to fan noise model results. The radial penalties used are described by Clark, Thomas, and Guo (Ref. 43). The front frame is assumed to consist of airfoil vanes ahead of the propulsor rotor. The additional noise of this arrangement is modeled by an inlet guide vane option contained in the Kontos method.

Jet noise of the aft propulsor is predicted using Stone's method as previously mentioned. For the special case of ST–ABL, the additional core noise of the turboshaft engine that drives the aft fan is predicted by the Emmerling method as previously mentioned. Noise levels of all components are predicted as lossless one-third octave band spectra and are summed in the vicinity of the airplanes prior to propagation.

The noise sources are analytically flown along takeoff and approach profiles computed using standards and procedures defined in Section 3.6 of Reference 34 as a guide. Profile calculations for takeoff and approach are performed at maximum gross weight and at maximum landing weight, respectively. The runway altitude is at sea level, and ambient temperature is 77 °F. The aft propulsors are used during takeoff and landing, as they are necessary to operate the airplanes properly. Maximum takeoff thrust is applied from brake release to a point just before the flyover noise monitor location, where a pilot-initiated thrust cutback is performed. Cutback thrust is determined by an amount that maintains a 4 percent climb gradient with all engines operating, or level flight with one engine inoperative. As noted in Section 3.3, for these models OEI results in a 50-percent reduction in available thrust even though this may not be strictly true for the actual vehicle. Cutback thrust is 67 and 62 percent of maximum takeoff-rated thrust for the STARC–ABL and ST–ABL concepts, respectively. Climbout speed is maintained at 20 kn over the takeoff safety speed. Flaps are deployed in the takeoff position throughout the procedure. The ST–ABL concept is lighter and has more total thrust than STARC–ABL. Because of this, ST–ABL reaches its takeoff safety speed earlier and climbs at a higher rate. The takeoff profiles of each vehicle are shown in Figure 17.

Flyover noise is evaluated on the extended runway centerline at a point 21,325 ft from brake release. Approach noise is evaluated at a point 6,562 ft before the runway threshold, when the aircraft are 394 ft above ground level. (The approach glide slope is 3°.) Lateral observers are located at points parallel to the extended runway centerline and displaced laterally by 1,476 ft. Maximum lateral noise is assumed to occur at sideline locations where the airplanes reach an altitude of 1,000 ft. At that point, airplanes are sufficiently high where refraction and scattering effects are small and additional lateral attenuation is negligible. The spectra are propagated to noise monitors located on the ground. Noise propagation effects include spherical spreading, Doppler shift and convective amplification, atmospheric absorption (Ref. 44), and ground reflections (Ref. 45) based on data for grass-covered ground (Ref. 46).
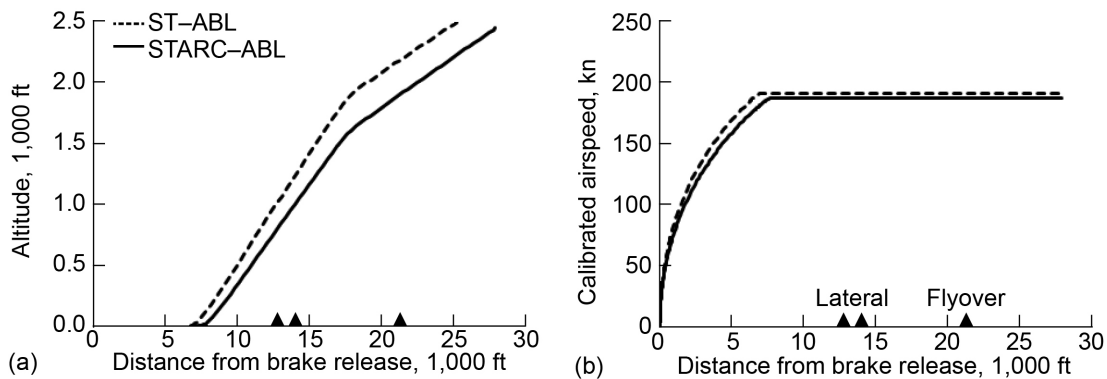

Figure 17.—Single-aisle turboelectric aircraft with aft boundary layer propulsion (STARC–ABL) and single-aisle transport aircraft with aft boundary layer propulsion (ST–ABL) takeoff profiles. (a) Altitude. (b) Calibrated airspeed.

4.0   Results

The primary objectives of this study included both evaluating the STARC–ABL EAP concept with new assumptions and methodologies and comparing STARC–ABL to ST–ABL to assess the importance of EAP to the STARC–ABL concept. As such, the following sections present characteristics of the STARC–ABL configuration, comparisons to the N3CC advanced conventional aircraft, and comparisons between STARC–ABL and ST–ABL.

4.1   Propulsion System

4.1.1   Overall Propulsion System and Turbomachinery

Table 3 to Table 5 contain the key propulsion system parameters for the N3CC, STARC–ABL, and ST–ABL; the difference between the N3CC and STARC–ABL; and the difference between the STARC–ABL and ST–ABL at the ADP, RTO, and midcruise conditions. The gray highlighted values indicate required thrust values or key design input values used in sizing the system.

A turbine engine's OPR, with all else being equal, determines the thermal efficiency of the core engine, with a higher OPR yielding a higher thermal efficiency. The maximum OPR is determined when either the corrected flow at the exit of the last compressor stage (Wc_3) reaches a minimum value (Wc_{3min}) at the ADP, or the total temperature at the exit of the last compressor stage (Tt_3) reaches a maximum value (Tt_{3max}) at any flight condition. For this study, the Wc_{3min} was set to be 2.5 lbm/s and the Tt_{3max} was set to 1,800 °R. With the engine sized at ADP such that Wc_3 equaled Wc_{3min}, the highest Tt_3 occurred at the RTO condition (Table 4). The Tt_3 at the RTO is less than 1,800 °R for all engines. This means that the OPR, and thus thermal efficiency, of all core engines in this study are determined by airflow coming into the core. The higher the airflow coming into the core, the higher the OPR can be before the Wc_3 reaches Wc_{3min}, and thus the higher the thermal efficiency of the core engine.

If the only difference between the STARC–ABL, ST–ABL, and N3CC cycles were the OPR of each system, then the TSFC of the "–ABL" systems would be higher than the N3CC because of their lower OPRs. This would have been especially true of the STARC–ABL where 10 percent of the power to drive the BLI propulsor is lost in the electrical transmission system. Because of the benefits of BLI, however, the STARC–ABL and ST–ABL systems overcome the impacts of a lower OPR and have a lower TSFC than the N3CC at the ADP and cruise conditions. It is certain that had all engines been limited by Tt_{3max}, and thus all are able to achieve the same OPR, the TSFC benefits of the STARC–ABL and ST–ABL systems compared to the N3CC would have been even greater than they are in this study. This is good motivation for looking at the benefits of fuselage BLI in a larger aircraft where the higher thrust levels would result in core airflows large enough that Tt_{3max} would be reached before the Wc_{3min} limit.

In the STARC–ABL cycle, a given amount of power extracted from the turbofan fan shaft by the generator and utilized by the BLI propulsor produces more thrust per horsepower than if that same amount of power were used to drive the fan in the turbofan engine. Thus, the best performance of the overall propulsion system is obtained when the BLI propulsor is operating at its maximum rated power. The STARC–ABL system, as currently configured, however, cannot operate with the BLI propulsor at full power during cruise. This is because the current STARC–ABL system uses a fixed pitch fan. The STARC–ABL system is sized at the ADP to drive the BLI propulsor motor at the rated power of 3,500 hp. However, as the turbine inlet temperature is reduced from climb power to cruise power and as altitude increases during cruise, the amount of shaft power generated by the LPT decreases. If the generator were to extract the same absolute amount of shaft power as it did at the ADP, the percentage of the LPT power going to the generator would increase and the percentage going to the fan would decrease.

TABLE 3.—COMPARISON OF PROPULSION SYSTEMS AT AERODYNAMIC DESIGN POINT (ADP)

ADP	N3CC[a]	STARC–ABL[b]	Percent change from N3CC[a] to STARC-ABL[b]	ST–ABL[c]	Percent change from STARC–ABL[b] to ST–ABL[c]
Flight condition					
Altitude, ft (m)	36,403 (11,096)	35,775 (10,904)	–1.7	34,950 (10,653)	–2.3
Mach number	0.785	0.785	0	0.785	0
Total propulsion system					
Thrust, lbf (kN)	7,310 (32.52)	7,357 (32.73)	0.6	7,221 (32.12)	–1.8
Thrust-specific fuel consumption, lbm/h/lbf (g/s/kN)	0.4785 (13.55)	0.4672 (13.23)	–2.4	0.4746 (13.44)	1.6
Equivalent bypass ratio	20.2	23.4	16	17.5	–25
Turbofan					
Thrust, lbf (kN)	3,655 (16.26)	2,401 (10.68)	–34	2,292 (10.20)	–4.5
Thrust turbofan/thrust total	0.50	0.33	–36	0.32	–1.1
Inlet airflow, lbm/s (kg/s)	480 (218)	304 (138)	–37	296 (134)	–2.6
Core airflow, lbm/s (kg/s)	22.6 (10.2)	19.6 (8.89)	–14	19.1 (8.66)	–2.6
Fan pressure ratio	1.30	1.30	0	1.30	0
Fan percent corrected speed	100	98.8	--------	100	--------
Compressor exit corrected flow, lbm/s (kg/s)	2.5 (1.13)	2.5 (1.13)	0	2.5 (1.13)	0
Compressor exit temperature, °R (K)	1,441 (801)	1,387 (711)	3.7	1,355 (753)	–2.3
Overall pressure ratio	46.7	38.6	–17	34.9	–9.6
Burner exit temperature, °R (K)	2,927 (1,626)	3,058 (1,699)	4.5	2,646 (1,470)	–13
Low-pressure turbine (LPT) power, hp (kW)	7,316 (5,455)	6,966 (5,195)	–4.8	4,910 (3,661)	–30
Fan power, hp (kW)	5,735 (4,277)	3,648 (2,720)	–36	3,575 (2,666)	–2.0
Generator power, hp (kW)	----------------	1,942 (1,448)	--------	----------------	--------
Generator power/LPT power	----------------	0.279	--------	----------------	--------
Turboshaft					
Thrust, lbf (kN)	----------------	--------	--------	90 (0.40)	--------
Inlet airflow, lbm/s (kg/s)	----------------	--------	--------	12.9 (5.851)	--------
Compressor exit corrected flow, lbm/s (kg/s)	----------------	--------	--------	2.5 (1.13)	--------
Overall pressure ratio	----------------	--------	--------	20.9	--------
Compressor exit temperature, °R (K)	----------------	--------	--------	1,182 (657)	--------
Burner exit temperature, °R (K)	----------------	--------	--------	2,775 (1,542)	--------
Output shaft power, hp (kW)	----------------	--------	--------	3,535 (2,636)	--------
Boundary layer ingestion (BLI) propulsor					
Thrust, lbf (kN)	----------------	2,556 (11.37)	--------	2,547 (11.33)	–0.4
Thrust BLI propulsor/thrust total	----------------	0.35	--------	0.35	0
Inlet airflow, lbm/s (kg/s)	----------------	345 (156.5)	--------	343 (155.6)	–0.6
Fan pressure ratio	----------------	1.25	--------	1.25	0
Percent fan corrected speed	----------------	100	--------	100	0
Fan power, hp (kW)	----------------	3,500 (2,610)	--------	3,500 (2,610)	0
Overall transmission system efficiency	----------------	90%	--------	99%	9

[a]N+3 conventional configuration (N3CC).
[b]Single-aisle turboelectric aircraft with aft boundary layer propulsion (STARC–ABL).
[c]Single-aisle transport aircraft with aft boundary layer propulsion (ST–ABL).

TABLE 4.—COMPARISON OF PROPULSION SYSTEMS AT ROLLING-TAKEOFF FLIGHT CONDITION

Rolling Takeoff (RTO)	N3CC[a]	STARC–ABL[b]	Percent change from N3CC[a] to STARC-ABL[b]	ST–ABL[c]	Percent change from STARC–ABL[b] to ST–ABL[c]
Flight condition					
Altitude, ft (m)	0	0	0	0	0
Mach number	0.255	0.258	1.2	0.26	0.8
Total propulsion system					
Thrust, lbf (kN)	34,512 (153.52)	34,113 (151.74)	–1.2	36,988 (164.53)	8.4
Thrust-specific fuel consumption, lbm/h/lbf (g/s/kN)	0.3124 (8.849)	0.3199 (9.061)	2.4	0.3242 (9.183)	1.3
Equivalent bypass ratio	20.9	20.2	–3.3	18.1	–11
Turbofan					
Thrust, lbf (kN)	17,256 (76.76)	14,673 (65.27)	–15	12,012 (53.43)	–18
Thrust turbofan/thrust total	0.50	0.43	–36	0.32	–1.1
Inlet airflow, lbm/s (kg/s)	1,281 (581.1)	859 (389.6)	–33	783 (355.2)	–8.8
Core airflow, lbm/s (kg/s)	58.5 (26.5)	58.0 (26.3)	–0.9	52.0 (23.6)	–10
Fan pressure ratio	1.26	1.36	8.6	1.39	2.2
Fan percent corrected speed	94.0	105.0	--------	94.6	--------
Compressor exit corrected flow, lbm/s (kg/s)	2.5 (1.1)	2.6 (1.2)	3.6	2.5 (1.1)	–2.0
Compressor exit temperature, °R (K)	1,729 (961)	1,683 (935)	–2.6	1,707 (948)	1.4
Overall pressure ratio	41.6	39.3	–5.5	36.0	–8.3
Burner exit temperature, °R (K)	3,400 (1,889)	3,400 (1,889)	0	3,251 (1,806)	–4.4
Low-pressure turbine power, hp (kW)	21,213 (15,819)	23,456 (17,491)	11	16,353 (12,194)	–30
Fan power, hp	16,626 (12,398)	15,474 (11,539)	–6.9	11,817 (8,812)	–24
Generator power, hp (kW)	------------------	1,942 (1,448)	-------	------------------	--------
Turboshaft					
Thrust, lbf (kN)	------------------	----------------	--------	600 (2.67)	--------
Inlet airflow, lbm/s (kg/s)	------------------	----------------	--------	34 (15.4)	--------
Compressor exit corrected flow, lbm/s (kg/s)	------------------	----------------	--------	2.49 (1.1)	--------
Overall pressure ratio	------------------	----------------	--------	20.8	--------
Compressor exit temperature, °R (K)	------------------	----------------	--------	1,454 (808)	--------
Burner exit temperature, °R (K)	------------------	----------------	--------	3,392 (1,884)	--------
Output shaft power, hp (kW)	------------------	----------------	--------	11,587 (8,640)	--------
Boundary layer ingestion (BLI) propulsor					
Thrust, lbf (kN)	------------------	4,767 (21.20)	--------	12,363 (54.99)	160
Thrust BLI propulsor/thrust total	------------------	0.14	--------	0.33	140
Inlet airflow, lbm/s (kg/s)	------------------	737 (334.3)	--------	1,032 (468.1)	40
Fan pressure ratio	------------------	1.086	--------	1.216	12
Percent fan corrected speed	------------------	65.3	--------	95	29.7
Fan power, hp (kW)	------------------	3,500 (2,610)	--------	11,472 (8,555)	230
Overall transmission system efficiency	------------------	90%		99%	9

[a]N+3 conventional configuration (N3CC).
[b]Single-aisle turboelectric aircraft with aft boundary layer propulsion (STARC–ABL).
[c]Single-aisle transport aircraft with aft boundary layer propulsion (ST–ABL).

TABLE 5.—COMPARISON OF PROPULSION SYSTEMS AT MIDCRUISE FLIGHT CONDITION

Midcruise	N3CC[a]	STARC–ABL[b]	Percent change from N3CC[a] to STARC–ABL[b]	ST–ABL[c]	Percent change from STARC–ABL[b] to ST–ABL[c]
Flight condition					
Altitude, ft	37,745 (11,505)	37,940 (11,564)	0.5	36,730 (11,195)	–4.1
Mach number	0.785	0.785	0	0.785	0
Total propulsion system					
Thrust, lbf (kN)	6,014 (26.75)	5,961 (26.52)	–0.9	6,758 (30.06)	13
Thrust-specific fuel consumption, lbm/h/lbf (g/s/kN)	0.4826 (13.67)	0.4693 (13.29)	–2.8	0.4726 (13.39)	0.7
Equivalent bypass ratio	20.8	24.0	15	17.7	–26
Turbofan					
Thrust, lbf (kN)	3,007 (13.38)	1,923 (8.55)	–36	2,158 (9.60)	12
Thrust turbofan/thrust total	0.50	0.32	18	0.32	0.0
Inlet airflow, lbm/s (kg/s)	436 (197)	267 (121)	–39	280 (127)	4.9
Core airflow, lbm/s (kg/s)	20.0 (9.7)	16.8 (7.6)	–16	18.0 (8.2)	7.1
Fan pressure ratio	1.27	1.28	0.3	1.30	1.6
Fan percent corrected speed	96.5	95.6	--------	100	--------
Compressor exit corrected flow, lbm/s (kg/s)	2.46 (1.12)	2.46 (1.12)	0	2.46 (1.12)	0
Compressor exit temperature, °R (K)	1,393 (774)	1,341 (745)	–3.7	1,344 (747)	0.2
Overall pressure ratio	43.2	36.0	–17	35.2	–2.2
Burner exit temperature, °R (K)	2,807 (1,559)	2,944 (1,636)	4.9	2,631 (1,462)	–11
Low-pressure turbine power, hp (kW)	6,115 (4,560)	5,681 (4,236)	–7.1	4,599 (3,429)	–19
Fan power, hp (kW)	4,768 (3,555)	2,956 (2,204)	–38	3,351 (2,499)	13
Generator power, hp (kW)	----------------	1,583 (1,180)	--------	----------------	--------
Generator power/low-pressure turbine power	----------------	0.279	--------	----------------	--------
Turboshaft					
Thrust, lbf (kN)	----------------	----------------	--------	47.2 (0.21)	--------
Inlet airflow, lbm/s (kg/s)	----------------	----------------	--------	11.87 (5.4)	--------
Compressor exit corrected flow, lbm/s	----------------	----------------	--------	2.5 (1.1)	--------
Overall pressure ratio	----------------	----------------	--------	20.5	--------
Compressor exit temperature, °R (K)	----------------	----------------	--------	1,163 (646)	--------
Burner exit temperature, °R (K)	----------------	----------------	--------	2,749 (1,527)	--------
Output shaft power, hp (kW)	----------------	----------------	--------	3,285 (2,450)	--------
Boundary layer ingestion (BLI) propulsor					
Thrust, lbf (kN)	----------------	2,116 (9.41)	--------	2,393 (10.64)	13
Thrust BLI propulsor/thrust total	----------------	0.35	--------	0.35	1.2
Inlet airflow, lbm/s (kg/s)	----------------	305 (138.3)	--------	324 (147.0)	6.2
Fan pressure ratio	----------------	1.23	--------	1.25	1.7
Percent fan corrected speed	----------------	97	--------	100	3.1
Fan power, hp (kW)	----------------	2,852 (2,127)	--------	3,252 (2,425)	14
Overall transmission system efficiency	----------------	90%	--------	99%	9

[a]N+3 conventional configuration (N3CC).
[b]Single-aisle turboelectric aircraft with aft boundary layer propulsion (STARC–ABL).
[c]Single-aisle transport aircraft with aft boundary layer propulsion (ST–ABL).

With a fixed pitch fan, the only way to reduce the amount of power absorbed by the fan is to run the fan at a lower speed. A lower fan shaft speed has a cascading effect that results in reduced overall core efficiency and increased TSFC. Since the low-pressure compressor (LPC) is on the same shaft as the fan, a reduction in corrected fan speed results in a reduction in corrected LPC speed. Reducing corrected LPC speed normally results in a reduced LPC flow rate and pressure ratio. However, the LPT needs to produce approximately the same amount of power since the total of the fan and generator power remains the same. Thus, the gas power coming into the LPT must not be reduced. This results in the high-pressure compressor (HPC) flow rate needing to remain at approximately the same level. This produces a flow mismatch between the LPC and HPC. To resolve this mismatch, the operating point on the LPC shifts off its line of peak efficiency and toward higher corrected flow and lower pressure ratio, while the HPC also shifts off its line of peak efficiency but towards lower corrected flow and higher pressure ratio. Shifting the operating points results in a reduction in efficiency in both compressors. Also, the need to produce the same amount of power at a lower shaft speed causes the LPT operating point to shift away from its peak efficiency line and to operate at a reduced efficiency. The reduction in the total efficiency of the turbofan core engine is larger than the propulsive efficiency improvement achieved by continuing to operate the BLI propulsor at its maximum power. The end result is that the total system TSFC increases for any operating point where the ratio of generator to LPT power is greater than it is at the ADP. Continuing to increase generator to LPT power ratio will eventually cause either the LPC to choke or the HPC to stall.

To avoid this situation, the generator power is limited such that the ratio of generator power to LPT power is never greater than it was for the maximum climb power at the ADP. The impact of this limitation is that the BLI propulsor operates at less than maximum rated power at the cruise condition, resulting in all of the cruise segment operating with less than the maximum BLI benefit possible. A potential solution would be to use a variable pitch fan, such as the one that Rolls-Royce LibertyWorks used in their Electrically Variable Engine^{TM} hybrid engine (Ref. 47). A variable pitch fan allows the fan power to be reduced without changing the shaft speed. This would enable the BLI motor to run at, or at least closer to, its maximum power during cruise, thus maximizing the BLI benefit.

4.1.2   Single-Aisle Turboelectric Aircraft With Aft Boundary Layer Propulsion (STARC–ABL) Electric Power Cable Analysis

For a given system voltage and transmitted power, the necessary current is given by $I = P/V$ where I is the current in amps, P is the power in watts, and V is the voltage. In sizing the STARC–ABL cables, the calculated current was multiplied by 1.3 to provide a margin of safety, but the power loss calculation used the actual current. With the margined amperage and the assumed current density (amps/area), the necessary cross-sectional area of the conductor can be calculated. The weight of the conductor is given by the density of the conductor times the cross-sectional area of the cable (A) times the length of the cable from the generator to the tailcone thruster motor and back to the generator (L). Since the requirements for insulation of high-voltage cables at high altitudes are still not determined, and since the weight of the insulation and jacket are small compared to the weight of the conductor, only the conductor weight was included in this analysis.

The cable is assumed to operate at 95 °C. The resistance of the cable from each generator to the motor and back to the generator is $R = R_sL/A$, where R_s is the specific resistivity in Ω-m and A in square meters and L in meters are as defined previously. The specific resistivity of aluminum at the given cable temperature is 3.28×10^{-8} Ω-m and that of copper is 2.04×10^{-8} Ω-m (Ref. 48). With the calculated resistance, the power loss in the cable is given by $P_{loss} = I^2R$. The transmission efficiency is then $\eta = P - P_{loss}/P$.

A key parameter in electrical cable sizing is selecting the number of amps per square inch to use. In this application, the assumption is that these cables will require active cooling and most likely some form

of liquid cooling. Liquid-cooled cables can carry far higher current densities than can uncooled cables (such as buried cables) or those cooled by natural convection. For this study, a current density of 1,500 A/in² is assumed for aluminum and 2,500 A/in² is assumed for copper.

The last two major design decisions to be made are the voltage of the electrical system and whether to use aluminum or copper as the conductor. Figure 18 and Figure 19 illustrate the variation in total cable weight and transmission efficiency as a function of system voltage for the selected current densities in these two different conductor materials. Significant reductions in weight, especially for copper, and power loss are possible with higher voltages. However, at all voltage levels the weight of the aluminum cable is substantially less than the copper. To be conservative until the safety and reliability of high-voltage cables at high altitudes is known, the decision was made to assume a system voltage of 1,000 V.

With the given current densities, the resistance of the aluminum cable is actually lower than the resistance of the copper cable. The transmission efficiency is higher because, while the specific resistivity of aluminum is 60 percent higher than that of copper, the lower current density used for aluminum results in a cross-sectional area for the aluminum cable that is 66 percent greater (1.2 in² for aluminum versus 0.72 in² for copper). Specific resistivity and cross-sectional area have an equal effect on resistance, thus the greater increase in cross section more than offsets the higher specific resistivity of aluminum.

If the current density of either the aluminum or copper cable changes, the cable with the higher transmission efficiency and lighter weight may change. It is possible that for different current densities, one type of cable could be lighter while the other type has higher transmission efficiency. Figure 20 gives the impacts of current density on cable weight and cable transmission efficiency for an aluminum cable in the STARC–ABL.

With lower weight and lower resistance, aluminum cables are the obvious choice for the STARC–ABL. The characteristics of an aluminum cable carrying 1.38 MW at 1,000 V are summarized in Table 6.
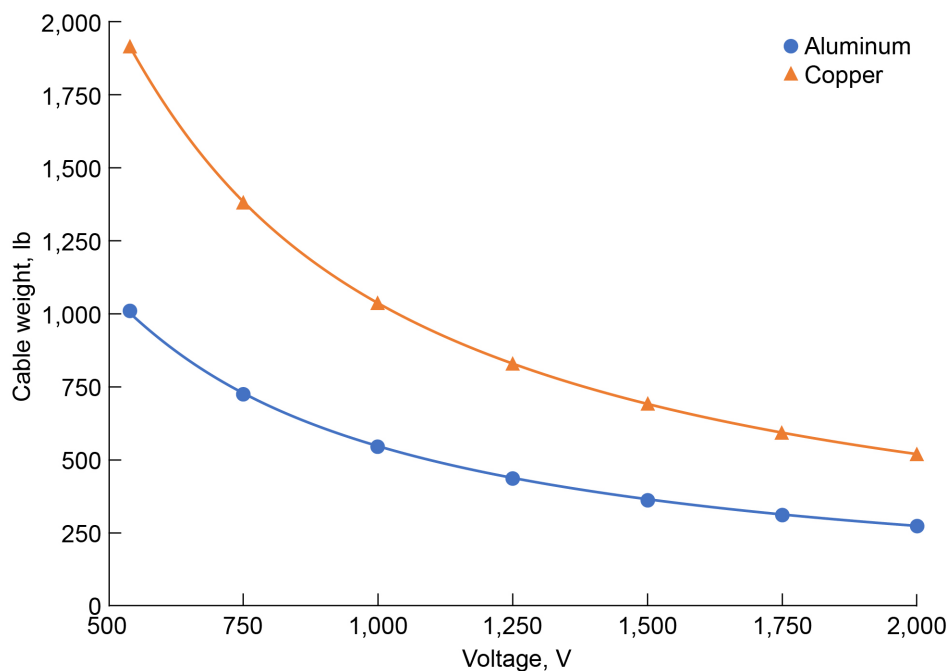

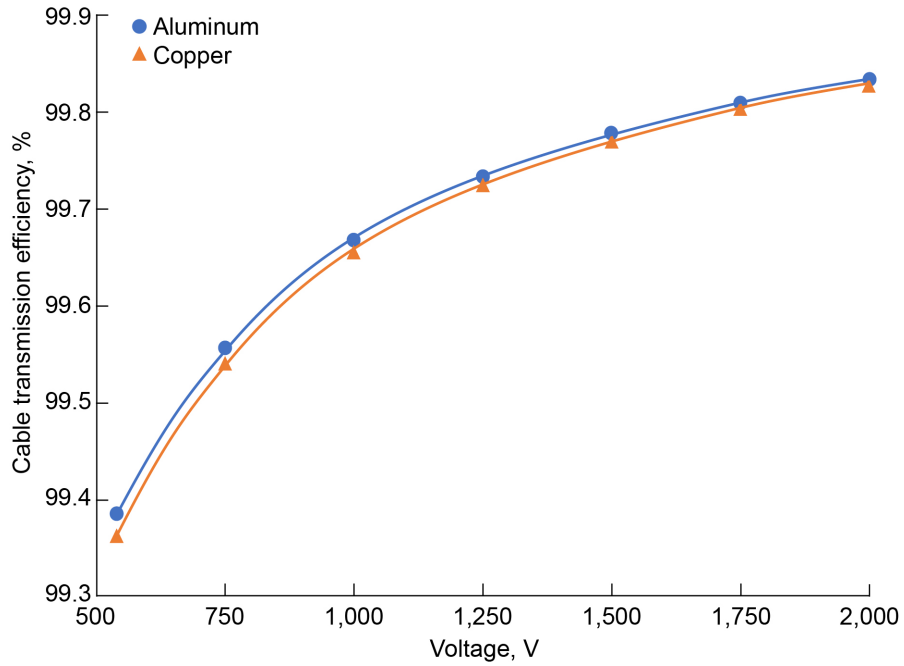Figure 18.—Total system cable weight versus voltage.

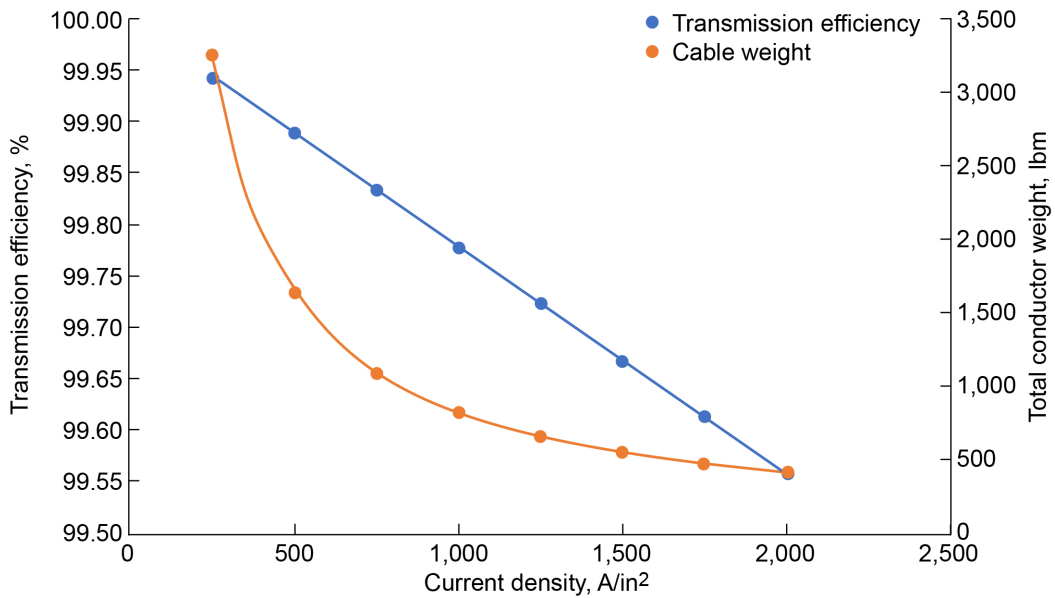Figure 19.—Cable transmission efficiency versus voltage.

Figure 20.—Variation of 1,000-V aluminum cable weight and transmission efficiency with current density.

TABLE 6.—ALUMINUM CABLE CHARACTERISTICS AT 1,000 V

Transmitted power (one generator to motor circuit), kW (hp) 1,378 (1,848)
Voltage, V 1,000
Current, A 1,378
Conductor cross section, in^2 (cm^2) 1.19 (7.68)
Conductor diameter, in. (cm) 1.23 (3.12)
Cable length (generator to motor to generator), ft (m) 186 (56.6)
Total cable weight (two cables), lb (kg) 545 (247)
Voltage drop, V 3.3
Power loss (one generator/motor/generator circuit), W (hp) 4,576 (6.14)
Total system power loss (two circuits), W (hp) 9,153 (12.27)
Transmission efficiency, percent 99.64

4.1.3 Single-Aisle Turboelectric Aircraft With Aft Boundary Layer Propulsion (STARC–ABL) Thermal Management System Analysis

The power levels, efficiencies, and resulting heat loads for the STARC–ABL electrical components are shown in Table 7. The total heat load of 388 hp combined with the TMS weight assumption of 2.3 hp rejected per pound calculated in Section 3.1.2.4 results in a TMS weight estimate of 169 lb.

4.1.4 Propulsion System Weight Analysis Results

A summary of the major weights for the N3CC, ST–ABL, and STARC–ABL propulsion systems is shown in Table 8.

A breakdown of the STARC–ABL electrical system weights is provided in Table 9. The weights for the motors, generators, rectifiers, and inverters were based on the assumed specific power for each component in Table 1. Electric cable weight is based on the analysis described in Section 4.1.2 and given in Table 6.

4.2 Mission Performance

The results of the N3CC, STARC–ABL, and ST–ABL sizing and performance analysis, the difference between the N3CC and the STARC–ABL, and the difference between the STARC–ABL and the ST–ABL are shown in Table 10. Overall, STARC–ABL has a similar gross weight to the N3CC but with reduced block fuel consumption. Propulsion system weight grew about 2 percent to accommodate the added electric propulsion and thermal management components, which drove empty weight up by 1 percent. A larger wing also contributes to this growth in empty weight. The propulsion system's fuel efficiency in cruise, as measured by TSFC, is about 2.6 percent better than the N3CC, resulting in a total block fuel reduction of 2.7 percent for the 900-nmi economic mission and 3.4 percent for the 3,500-nmi design mission. It is clear that STARC–ABL's benefit improves with longer mission lengths, due to the concept's improved cruise efficiency. Other metrics are not substantially different between the N3CC and STARC–ABL.

Because it does not need additional electric components, ST–ABL's propulsion system is 8.8 percent lighter than STARC–ABL's, which contributes to a small reduction in empty weight. Despite this weight reduction, sea-level static (SLS) thrust was dramatically increased in ST–ABL, about 24 percent more than STARC–ABL. This dramatic difference in SLS thrust was unexpected and was investigated through further analysis. ST–ABL's fuel efficiency, measured as TSFC, is 1.8 percent worse than STARC–ABL's. Compounded over the length of a mission, this leads to a substantial increase in block fuel for both the design and economic missions.

TABLE 7.—HEAT LOADS FOR SINGLE-AISLE TURBOELECTRIC AIRCRAFT
WITH AFT BOUNDARY LAYER PROPULSION (STARC–ABL)
ELECTRICAL COMPONENTS

Component	Power into device, hp (MW)	Efficiency, percent	Heat load, hp (kW)
Generators (shaft input)	3,889 (2.90)	96	155 (116)
Rectifiers	3,733 (2.78)	99	37 (27.8)
Cable	3,696 (2.76)	99.67	12 (9.1)
Inverter	3,684 (2.75)	99	37 (27.5)
Motor	3,647 (2.72)	96	146 (109)
Motor shaft output	3,500 (2.61)	--------	------------
Total	--------------	90	388 (289)

TABLE 8.—PROPULSION SYSTEM WEIGHTS

N3CC[a]		STARC–ABL[b]		ST–ABL[c]	
Component	lb (kg)	Component	lb (kg)	Component	lb (kg)
Underwing turbofans	12,014 (5,449)	Underwing turbofans	8,154 (3,699)	Underwing turbofans	7,550 (3,425)
------------------------	-----------------	Electrical system	2,108 (956)	Turboshaft engine	1,607 (729)
------------------------	-----------------	Boundary layer ingestion (BLI) propulsor	1,828 (829)	BLI propulsor	2,061 (935)
------------------------	-----------------	Thermal management system	169 (77)	------------------------	-----------------
Total	12,014 (5,449)	Total	12,259 (5,561)	Total	11,218 (5,088)

[a]N+3 conventional configuration (N3CC).

[b]Single-aisle turboelectric aircraft with aft boundary layer propulsion (STARC–ABL).

[c]Single-aisle transport aircraft with aft boundary layer propulsion (ST–ABL).

TABLE 9.—SINGLE-AISLE TURBOELECTRIC AIRCRAFT WITH
AFT BOUNDARY LAYER PROPULSION (STARC–ABL)
ELECTRICAL SYSTEM WEIGHTS

Component	Power into device, hp (MW)	Specific power, hp/lb (kW/kg)	Weight, lb (kg)
Generator (shaft input)	3,889 (2.90)	8.0 (13.2)	486 (221)
Rectifiers	3,733 (2.78)	11.6 (19.1)	322 (146)
Cables	3,696 (2.76)	-------------	545 (247)
Inverter	3,683 (2.75)	11.6 (19.1)	319 (145)
Motor (electric power input)	3,646 (2.72)	-------------	----------------
Motor (shaft output)	3,500 (2.61)	8.0 (13.2)	438 (198)
Total	---------------	-------------	2,108 (956)

TABLE 10.—STARC–ABL[a] PERFORMANCE COMPARED TO N3CC[b] AND ST–ABL[c] PERFORMANCE

Parameter	N3CC[b]	STARC–ABL[a]	ST–ABL[c]	Percent change from N3CC[b] to STARC–ABL[a]	Percent change from ST–ABL[c] to STARC–ABL[a]
Cruise Mach	0.785	0.785	0.785	-------	-------
Propulsion system weight, lb (kg)	12,620 (5,724)	12,870 (5,838)	11,740 (5,325)	2.0	–8.8
Operating empty weight, lb (kg)	77,780 (35,280)	78,580 (35,643)	77,370 (35,094)	1.0	–1.5
Takeoff gross weight, lb (kg)	134,880 (61,181)	134,830 (61,158)	134,310 (60,922)	–0.03	–0.39
Maximum thrust (sea-level static), lb (kN)	43,320 (192.7)	42,830 (190.52)	53,250 (236.87)	–1.1	24.3
Wing area, ft^2 (m^2)	1,119 (104.0)	1,135 (105.4)	1,097 (101.9)	1.4	–3.4
Thrust specific fuel consumption (start of cruise), lbm/h/lbf (kg/h/N)	0.480 (0.04895)	0.468 (0.04772)	0.476 (0.04854)	–2.6	1.8
Lift over drag (start of cruise)	20.7	21.0	20.8	1.6	–1.0
Takeoff field length, ft (m)	8,200 (2,499)	8,200 (2,499)	7,490 (2,283)	0.0	–8.6
Landing field length, ft (m)	6,120 (1,865)	6,050 (1844)	6,190 (1,887)	–1.0	2.3
Approach velocity, kn (km/h)	149 (240)	148 (238)	150 (241)	–0.67	1.5
Block fuel (design mission), lb (kg)	23,360 (10,596)	22,560 (10,233)	23,120 (10,487)	–3.4	2.5
Block fuel (economic mission), lb (kg)	6,410 (2,908)	6,240 (2,830)	6,540 (2,966)	–2.7	4.9

[a] Single-aisle turboelectric aircraft with aft boundary layer propulsion (STARC–ABL).
[b] N+3 conventional configuration (N3CC).
[c] Single-aisle transport aircraft with aft boundary layer (ST–ABL).

Comparisons of mission profiles for the N3CC baseline, STARC–ABL, and ST–ABL are shown in Figure 21 and Figure 22. The variation in the profiles is primarily caused by differences in climb performance between the aircraft. STARC–ABL is notable for having the highest TOC altitude, allowing it to have the highest cruise altitude, whereas ST–ABL consistently has the lowest altitudes in any phase of flight.
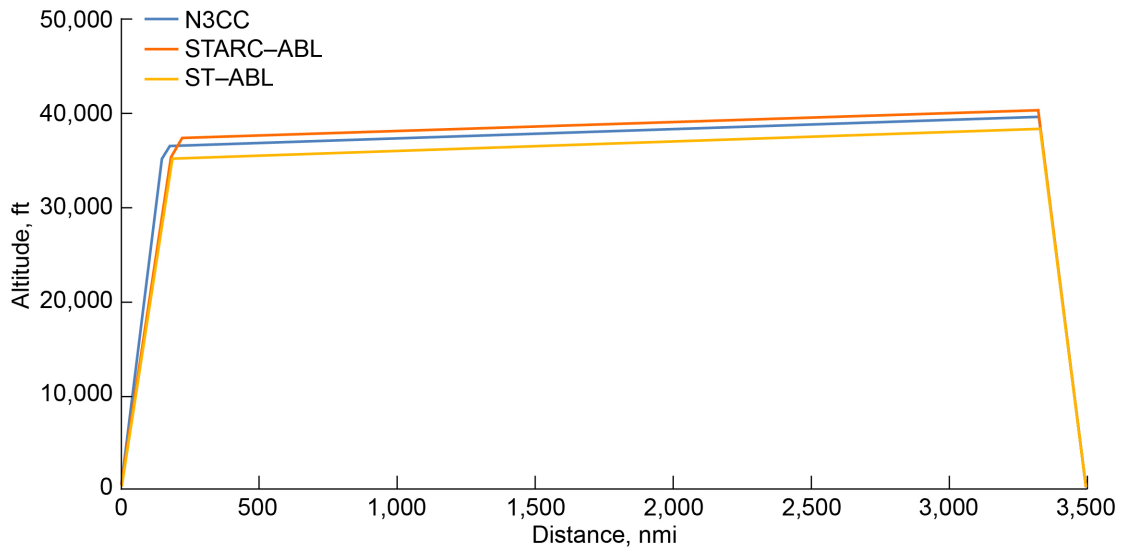
Figure 21.—Altitude profiles for 3,500-nmi design mission. N+3 conventional configuration (N3CC). Single-aisle transport aircraft with aft boundary layer propulsion (ST–ABL). Single-aisle turboelectric aircraft with aft boundary layer propulsion (STARC–ABL).
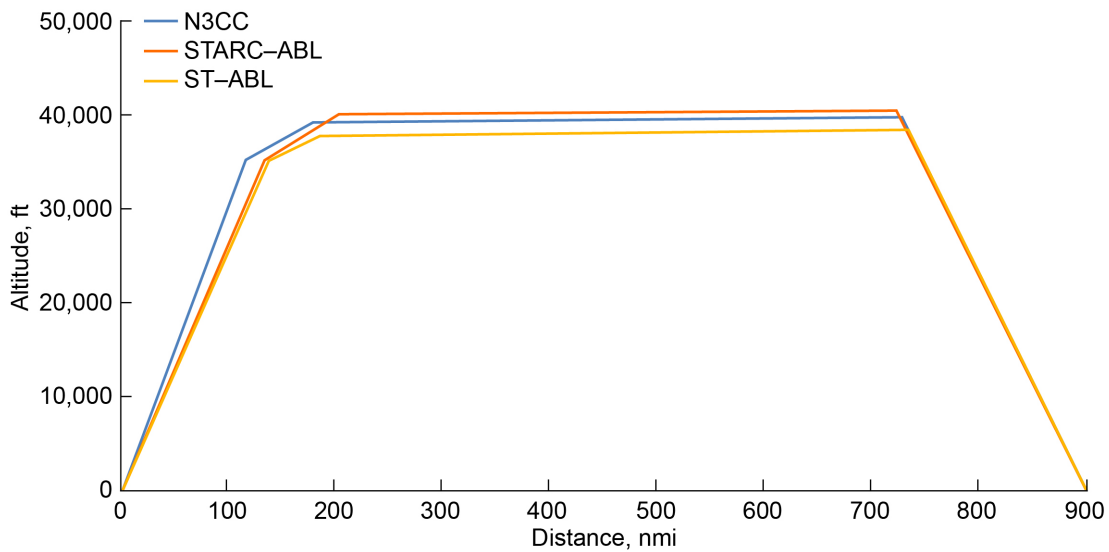

Figure 22.—Altitude profiles for 900-nmi economic mission. N+3 conventional configuration (N3CC). Single-aisle transport aircraft with aft boundary layer propulsion (ST–ABL). Single-aisle turboelectric aircraft with aft boundary layer propulsion (STARC–ABL).

The variation in climb performance is partially driven by the constraints set on vehicle performance, which can be better visualized through a comparison of constraint diagrams. Shown in Figure 23, these plots show feasible combinations of thrust and wing area (which set thrust and wing loading) when constrained by operational limitations. Shaded regions show design points that are not valid because they violate a specific constraint, and the plot is overlaid with contour lines of block fuel. The design point for each vehicle is marked on each plot. The STARC–ABL design point is dominated by the takeoff field length requirement, which drives both thrust and wing area. The vehicle is not limited by any of the constraints evaluated at TOC. Conversely, ST–ABL is not limited by takeoff field length, but instead it

has thrust constrained by excess power requirements and wing area by approach velocity. There is a clear difference in aircraft behavior with respect to altitude, with STARC–ABL being driven by sea-level performance and ST–ABL limited by performance at altitude.

ST–ABL clearly has more SLS thrust than required to meet design constraints, as demonstrated by the takeoff field length constraint not being active. Table 11 shows that although ST–ABL produces 24 percent more thrust than STARC–ABL at sea level, at 35,000 ft, ST–ABL produces 7 percent less thrust. At this flight condition, ST–ABL has reached the 300 ft/min specific excess power constraint and can no longer climb, but STARC–ABL has 740 ft/min of specific excess power and has significant margin to continue climbing to over 37,000 ft.
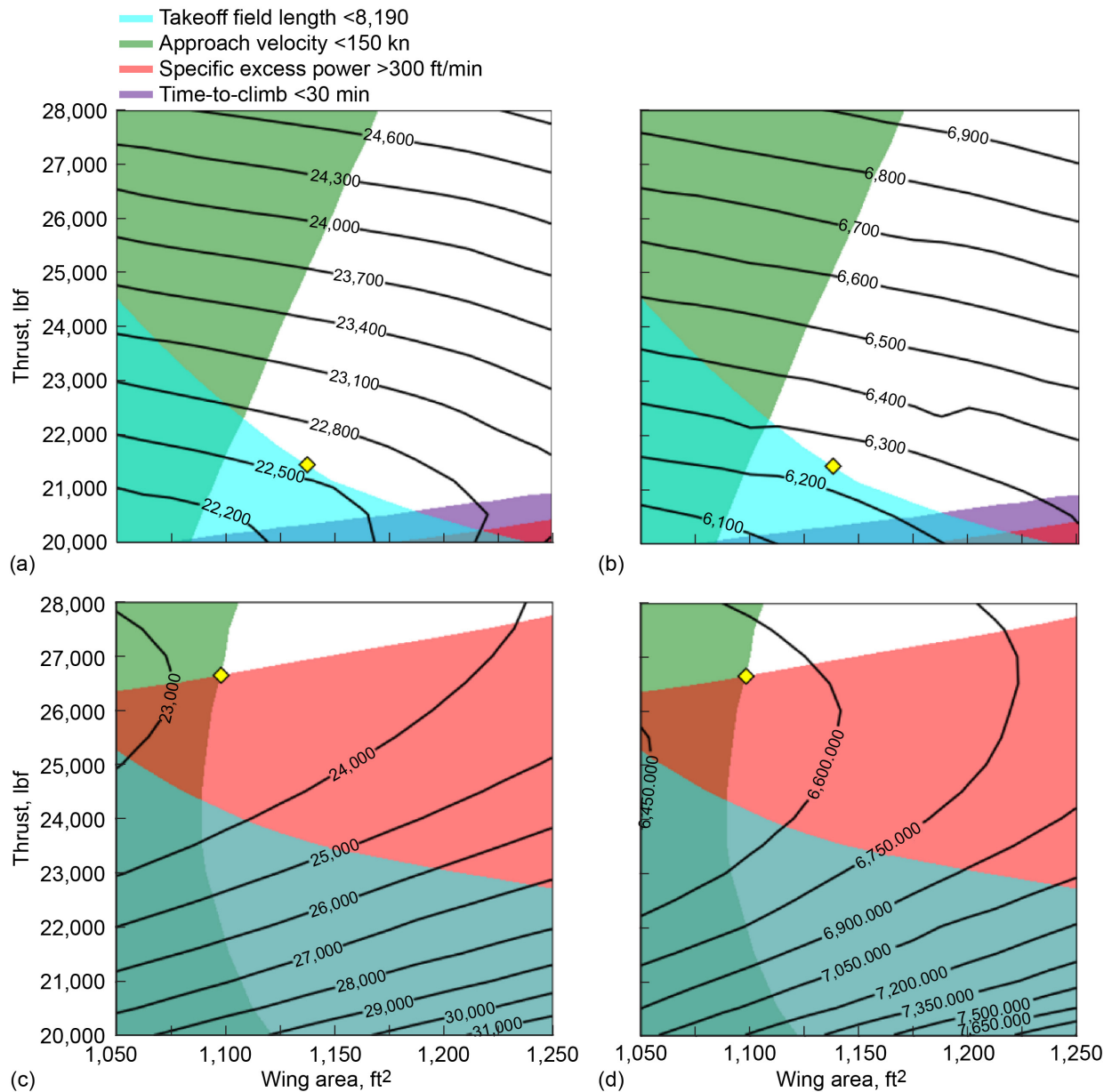

Figure 23.—Constraint diagrams of single-aisle turboelectric aircraft with aft boundary layer propulsion (STARC–ABL) and single-aisle transport aircraft with aft boundary layer propulsion (ST–ABL). STARC–ABL block fuel (a) design mission and (b) economic mission. ST–ABL block fuel (c) design mission and (d) economic mission.

TABLE 11.—COMPARISON OF THRUST PERFORMANCE

Parameter	STARC–ABL[a]	ST–ABL[b]	Percent change from STARC–ABL[a] to ST–ABL[b]
Sea-level static (SLS) maximum thrust, lbf (kN)	42,830 (190.5)	53,250 (236.9)	24.3
Top-of-climb maximum thrust, 35,000 ft, lbf (kN)	7,730 (34.4)	7,180 (31.9)	–7.1
Thrust to weight ratio, SLS	0.317	0.396	24.8

[a]Single-aisle turboelectric aircraft with aft boundary layer propulsion (STARC–ABL).
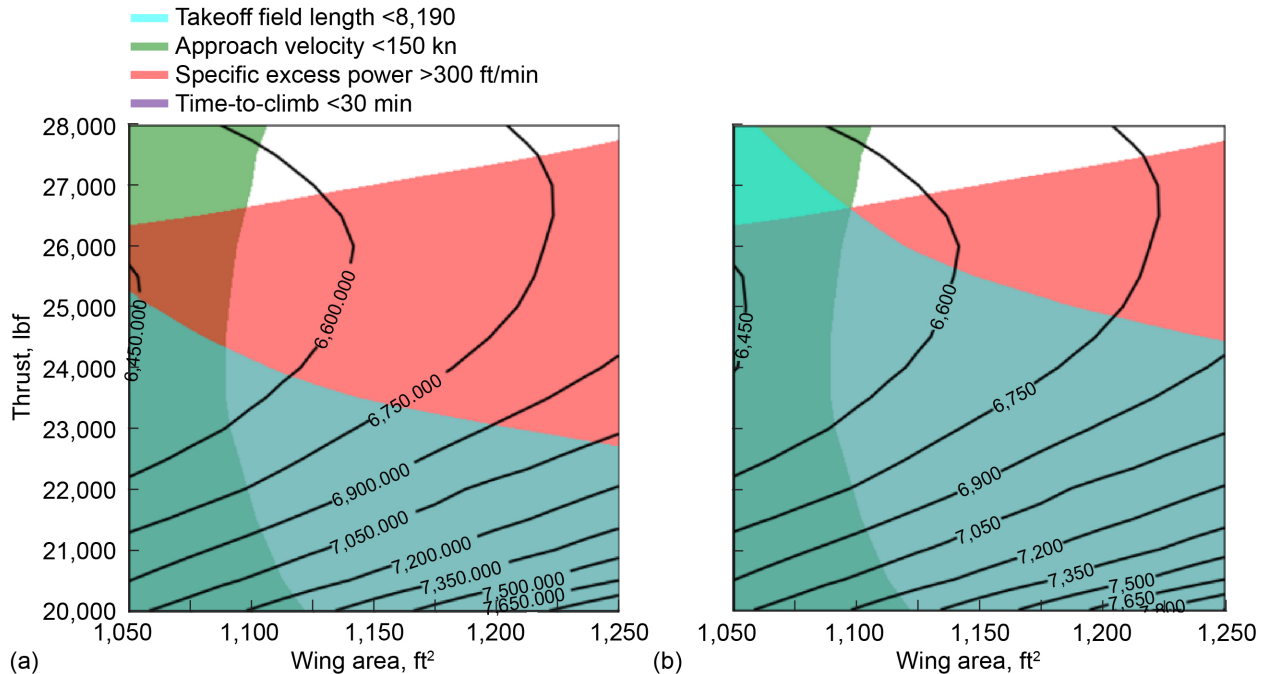[b]Single-aisle transport aircraft with aft boundary layer propulsion (ST–ABL).

Figure 24.—Single-aisle transport aircraft with aft boundary layer propulsion (ST–ABL) constraint diagrams (a) before and (b) after takeoff thrust reduction.

This extreme difference in performance may be explained through differences in thrust lapse rate between the vehicles. The additional thrust produced by ST–ABL at sea level comes from the BLI propulsor. The turboshaft is sized to provide 3,500 hp at TOC, but at sea level, the same turboshaft is able to produce over 11,000 hp. Conversely, for STARC–ABL, the BLI propulsor is powered at 3,500 hp for both the TOC and sea-level conditions.

It was hypothesized that the difference in low-altitude performance might have affected ST–ABL's design point through a compromise in engine cycle design. If ST–ABL's propulsion system was designed with an excessively high sea-level thrust target, some elements of the cycle design may have been penalized in order to meet this requirement. To determine if this impacted ST–ABL performance, a test was created. The thrust used by FLOPS to determine takeoff performance was derated until the takeoff field length constraint was matched. This modification did not change the thrust levels used for mission analysis (climb, cruise, descent, and reserve) so mission performance remained unchanged. Takeoff thrust needed to be reduced by 8 percent before takeoff field length equaled the 8,190 ft constraint. Figure 24 shows the constraint diagrams of the original ST–ABL model compared to the model with reduced takeoff thrust before engine resizing. The takeoff field length constraint becomes relevant, but this did not change the design point in a meaningful way.

This reduced sea-level thrust target was used with the same TOC thrust to resize the propulsion system. Propulsion system performance was not significantly affected and both TOC and SLS thrust remained approximately the same as the original design, with SLS thrust being much higher than needed to satisfy low-altitude performance constraints. This demonstrated that TOC thrust was driving propulsion system sizing and sea-level performance was not limiting cycle design. In other words, the high sea-level thrust could not be reduced while still meeting required performance at altitude. The conclusion from this experiment was that the differences in low-altitude performance between ST–ABL and STARC–ABL are due to the unique characteristics of their propulsion systems. ST–ABL performance could theoretically be improved by not using all available power during takeoff and climb at low altitudes. This could save some fuel and potentially reduce wear on the engines to save on maintenance costs, but these operational benefits were not explored in this study. Because this test showed no practical effect on ST–ABL's design point, the model variants created with derated sea-level thrust were not used to generate any results presented in this report.

4.3 Noise Characteristics

Noise predictions appropriate for transport category airplanes were made for the STARC–ABL and ST–ABL concepts. Inputs to the component noise prediction methods described earlier are engine and airframe data as functions of vehicle state and flight condition. Engine-state data at the noise measurement conditions for the STARC–ABL and ST–ABL propulsion systems are shown in Table 12 and Table 13, respectively.

TABLE 12.—SINGLE-AISLE TURBOELECTRIC AIRCRAFT WITH AFT BOUNDARY LAYER
PROPULSION (STARC–ABL) ENGINE DATA AT NOISE MEASUREMENT CONDITIONS

Parameter	Lateral Mach = 0.288, 1,000 ft (305 m)	Flyover Mach = 0.293, 1,900 ft (579 m)	Approach Mach = 0.198, 394 ft (120 m)
Underwing engines			
Net thrust per engine, lbf (kN)	13,760 (61.2)	8,240 (36.7)	2,870 (12.8)
Fan shaft speed, rpm	4,140	3,470	2,190
Fan airflow, lbm/s (kg/s)	845 (383)	720 (327)	500 (227)
Fan pressure ratio	1.36	1.23	1.07
Core nozzle pressure ratio	1.33	1.18	1.05
Core nozzle jet velocity, ft/s (m/s)	1,200 (366)	880 (268)	450 (137)
Bypass nozzle pressure ratio	1.42	1.28	1.09
Bypass nozzle jet velocity, ft/s (m/s)	820 (250)	690 (210)	410 (125)
Tailcone propulsor			
Net thrust, lbf (kN)	4,490 (20.0)	4,400 (19.6)	3,540 (15.7)
Fan shaft speed, rpm	2,260	2,280	1,910
Fan pressure ratio	1.09	1.09	1.06
Fan airflow, lbm/s (kg/s)	730 (331)	720 (327)	630 (286)
Nozzle jet velocity, ft/s (m/s)	500 (152)	500 (152)	380 (116)

TABLE 13.—SINGLE-AISLE TRANSPORT AIRCRAFT WITH AFT BOUNDARY LAYER
PROPULSION (ST–ABL) ENGINE DATA AT NOISE MEASUREMENT CONDITIONS

Parameter	Lateral Mach = 0.288, 1,000 ft (305 m)	Flyover Mach = 0.293, 1,900 ft (579 m)	Approach Mach = 0.198, 394 ft (120 m)
Underwing engines			
Net thrust per engine, lbf (kN)	11,230 (50.0)	4,510 (20.1)	1,630 (7.3)
Fan shaft speed, rpm	3,970	2,950	1,990
Fan airflow, lbm/s (kg/s)	780 (354)	590 (268)	430 (195)
Fan pressure ratio	1.30	1.14	1.06
Core nozzle pressure ratio	1.37	1.12	1.04
Core nozzle jet velocity, ft/s (m/s)	1,240 (378)	690 (210)	380 (116)
Bypass nozzle pressure ratio	1.36	1.20	1.07
Bypass nozzle jet velocity, ft/s (m/s)	760 (232)	580 (177)	350 (107)
Tailcone propulsor			
Net thrust, lbf (kN)	11,420 (50.8)	10,890 (48.4)	5,680 (25.3)
Fan shaft speed, rpm	3,030	3,020	2,170
Fan pressure ratio	1.22	1.22	1.09
Fan airflow, lbm/s (kg/s)	1,020 (463)	980 (445)	770 (349)
Nozzle jet velocity, ft/s (m/s)	690 (210)	690 (210)	460 (140)

Noise predictions for both concepts are shown in Figure 25. In the figure, published noise type certificate data of Chapter 4 (Ref. 34) aircraft are shown for comparison. Chapter 3 and Chapter 4 (Ref. 34) limits for trijets are also plotted in the figure. Since the fuselage BLI propulsors are designed to be thrust producing, necessary equipment in all phases of flight, STARC–ABL and ST–ABL are considered to be trijets with respect to noise regulations. Even if the BLI propulsors were not designed to be dispatch critical, the concepts are somewhat unconventional, and they would be regulatory oddities. It is not obvious, therefore, if future regulators would classify these aircraft as two-engine or three-engine aircraft, or whether STARC–ABL and ST–ABL would be classified the same. It is possible that ST–ABL might even be considered a four-engine aircraft because of the additional exhaust of its turboshaft engine. Recall that because of the approach used to model the propulsion systems in FLOPS, both STARC–ABL and ST–ABL are treated as two-engine aircraft in the calculation of the takeoff trajectories, with half the available thrust assumed lost in the case of one engine being inoperative.

Cumulative noise margins to Chapter 4 (Ref. 34) limits for the STARC–ABL and ST–ABL concepts are predicted to be 14 and 12 EPNdB, respectively. Chapter 14 (Ref. 34) margins are 7 and 5 EPNdB. At all three noise measurement conditions, the loudest noise source of the ST–ABL concept is its BLI propulsor. The ST–ABL BLI propulsor spins more rapidly and creates more thrust (and noise) than the STARC–ABL propulsor due to the lapse behavior of its turboshaft engine as discussed earlier. The additional noise sources attributed to distorted inflow and the front frame are responsible for the loud BLI propulsor. The BLI propulsor is the loudest source of noise of the STARC–ABL concept only at the approach condition. Fan noise of the underwing engines is the loudest source of noise at the lateral and flyover conditions. Jet noise is not a significant source for either concept due to the low nozzle pressure ratios associated with high bypass ratio engines. The ST–ABL turboshaft engine is only a minor contributor to the ST–ABL noise.
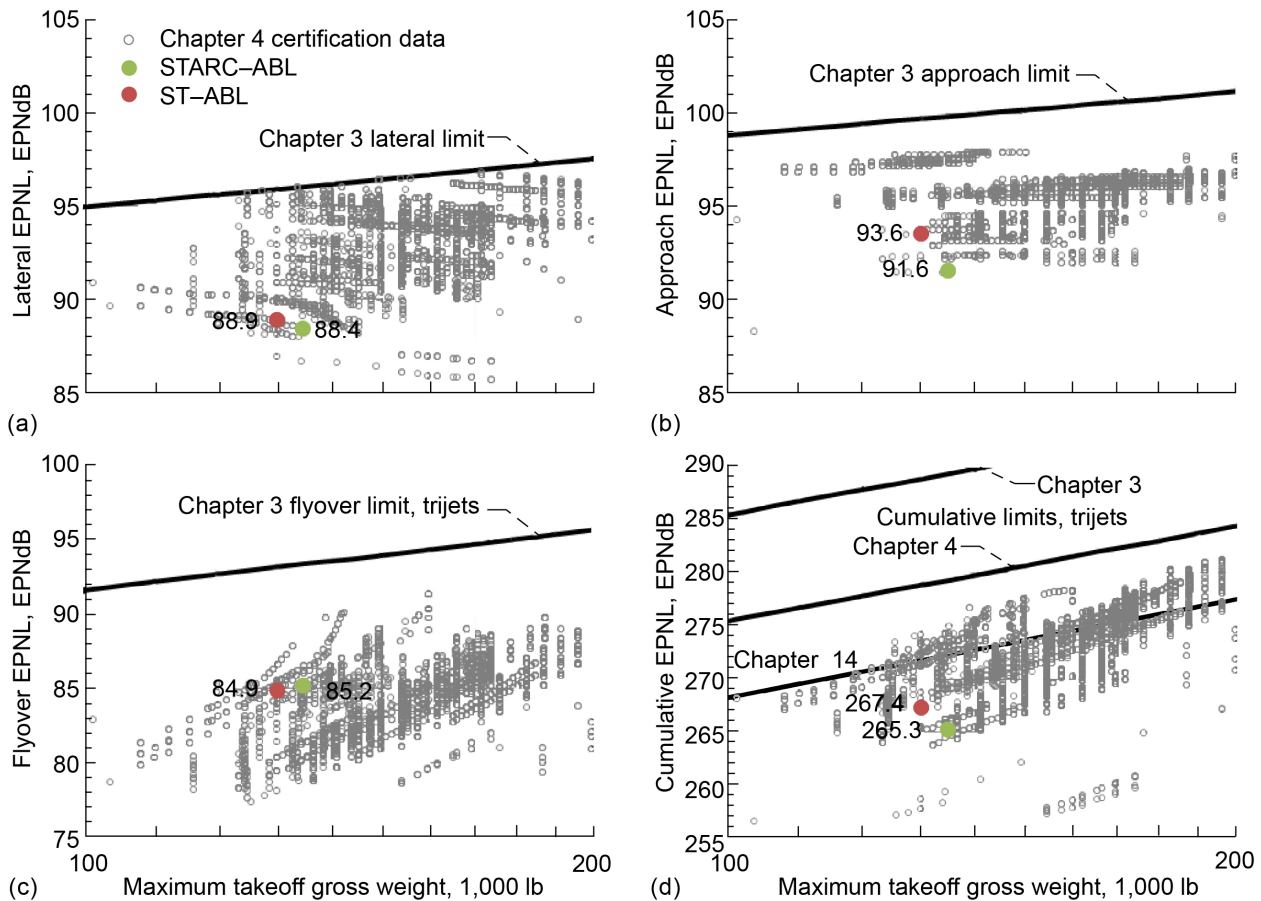
Figure 25.—Predicted certification noise levels for single-aisle turboelectric aircraft with aft boundary layer propulsion (STARC–ABL) and single-aisle transport aircraft with aft boundary layer propulsion (ST–ABL). (a) Lateral effective perceived noise level (EPNL). (b) Approach EPNL. (c) Flyover EPNL. (d) Cumulative EPNL.

Although the aft propulsors are a significant noise source, it does not seem to disqualify the concepts from a noise perspective. Owing to their advanced, high bypass underwing turbofans, the STARC–ABL and ST–ABL concepts are predicted to be comparable with other aircraft, despite the additional noise of their aft propulsors. Uncertainty at this stage of analysis, however, is high as actual noise levels could be significantly higher than the predicted values. An uncertainty analysis should be performed to identify the key areas of uncertainty.

5.0   Summary of Results

Electrified aircraft propulsion (EAP) has generated significant interest and excitement over the past several years. In addition to providing the potential to use stored carbon-neutral/carbon-free terrestrial energy for aircraft propulsion, EAP opens new propulsion integration flexibilities that are difficult to implement with conventional propulsion systems. This report has investigated the potential benefits of the single-aisle turboelectric aircraft with aft boundary layer propulsion (STARC–ABL) concept, which includes the combination of EAP (in the form of a partially turboelectric architecture) with fuselage boundary layer ingestion (BLI) propulsion. EAP enables power to be supplied to the BLI propulsor by means of electrical cables rather than mechanical shafting. There are, however, losses associated with the turboelectric system that partially offset the benefits. This report provided an update to the initial

investigation of STARC–ABL reported in 2016. In addition to a change in the design mission, the propulsion analysis methodology has been improved. The updated fuel consumption benefits predicted for STARC–ABL are significantly less than the original 2016 study. For the 3,500-nmi design mission, STARC–ABL is predicted to consume 3.4 percent less fuel than an equivalent technology conventional vehicle. The benefit drops to 2.7 percent for the 900-nmi economic mission. Previously reported benefits were 12.2 and 6.8 percent for the 3,500- and 900-nmi missions, respectively. Most of the benefit reduction can be traced to corrections made in the propulsion analysis methodology. The updated fuel consumption benefit estimates for STARC–ABL are similar to predictions by others who have evaluated the concept.

In order to determine if the EAP solution used in the STARC–ABL results in higher fuel savings than using a separate turbine engine to directly drive the BLI propulsor, a third aircraft, the single-aisle transport aircraft with aft boundary layer propulsion (ST–ABL), was added to the study. The transmission efficiency for the ST–ABL BLI propulsor is 99 percent, considerably higher than the 90 percent transmission efficiency for the STARC–ABL BLI propulsor. However, the overall pressure ratio (OPR) of the ST–ABL turbofan is 35, compared to an OPR of 39 for the STARC–ABL. In addition, the turboshaft engine, which is unique to the ST–ABL and which produces about a quarter of the total propulsion system shaft power, has an OPR of 21. In aggregate, the ST–ABL has a lower thermal efficiency than the STARC–ABL. The combined effect of these two factors, and other more difficult to quantify factors like a significant difference in altitude lapse rates of the two propulsion systems, results in ST–ABL having a 2.9 percent greater fuel consumption than STARC–ABL for the 3,500-nmi design mission and 4.9 percent greater fuel consumption for the 900-nmi economic mission.

The current study also included estimates of noise characteristics of the concepts, which were not part of the 2016 study. Cumulative noise margins relative to current regulatory limits were predicted to be 7 and 5 dB for the STARC–ABL and ST–ABL, respectively. The additional noise of the aft propulsor did not seem to disqualify the concepts, though uncertainty is high at this stage of analysis. Owing to their high bypass underwing turbofans, the STARC–ABL and ST–ABL concepts were predicted to be comparable with other aircraft, despite the additional noise of their aft propulsors.

With the assumptions made in this current study for the EAP component weights and efficiencies, the turboelectric STARC–ABL approach to fuselage BLI provides small, but not insignificant, improvements in both fuel consumption and noise compared to a conventional aircraft. It also shows that an EAP approach to driving a BLI propulsor yields greater fuel savings than using a separate turbine engine that uses a drive shaft to mechanically drive the BLI propulsor.

5.1   Future Work

Although this updated study has provided a better understanding of the STARC–ABL concept, there are still a number of improvements that could be made to the analysis. The use of integrated computational fluid dynamics (CFD) and propulsion analysis to estimate the power savings coefficient of the BLI propulsor is a significant improvement over the superposition approach used previously. However, the power saving coefficient used in the current analysis is for an idealized, isolated fuselage. The power savings coefficient values in the propulsion system analysis need to be updated to reflect more recent CFD analyses incorporating the effects of fuselage upsweep and wing downwash. The addition of a variable pitch fan to the turbofans in the STARC–ABL configuration would expand the operating space of the engine to yield better stability and efficiency. By being able to decouple, to a degree, the fan load and the fan speed, a variable pitch fan allows the fan shaft speed and load to be varied separately in order to find an optimum set of operating conditions for all of the turbomachinery and the generator power (which affects the amount of boundary layer that is ingested by the BLI propulsor), such that the lowest possible thrust-specific fuel

consumption for a given thrust level, altitude, and flight speed can be obtained. A variable pitch fan would enable the generator to operate at maximum power for more flight conditions and power settings by making it possible to reduce the fan load without reducing shaft speed. Maximizing generator power is desirable since the BLI propulsor produces more thrust per horsepower than the underwing engines, and thus, there is an advantage to keeping power to the BLI propulsor as high as possible. Another benefit of a variable pitch fan is that it eliminates the need for a variable area bypass nozzle, which is otherwise required to maintain fan stability. It may also be possible to eliminate the thrust reverser if a variable pitch fan is used.

The motor, generators, and power electronics in the STARC–ABL electrical system were modeled with simple specific power assumptions and constant efficiencies. A potential improvement in future studies would be to develop an electrical machine sizing algorithm that can calculate the weight from specified design parameters and then estimate the design efficiency of the machine and either calculate the efficiency map or use the design efficiency to calculate a scaler to be applied to an existing map to estimate off-design performance. A much more detailed analysis is required to determine the dynamics and operability of the electrical system. The thermal management system modeling would also benefit from enhancement to provide a more detailed estimate of the system weight, power, and drag impacts.

The STARC–ABL concept has only been evaluated for a single-aircraft size class. It is not clear how the benefits would change for larger or smaller aircraft. Since the benefit of the BLI propulsor is primarily in cruise, it is expected that larger aircraft with longer cruise ranges could see additional overall benefit. Furthermore, for larger aircraft with larger engines, the OPR of the turbofan engines would likely be limited by the maximum compressor exit total temperature (Tt_{3max}) rather than the minimum compressor exit corrected flow (Wc_{3min}). The result would be that, unlike the turbofans in this study, the STARC–ABL and N3CC turbofans would have the same OPR, and thus, equal core engine thermal efficiency. If the turbofans and turboshaft in the ST–ABL configuration were also limited by Tt_{3max} instead of Wc_{3min}, then the thermal efficiency would not suffer by the use of three lower flow rate core engines. With a higher transmission efficiency and without the penalties of smaller core engines, the ST–ABL configuration may yield greater fuel consumption reduction than the STARC–ABL for large aircraft.

There are options for powering the fuselage BLI propulsor in ways other than the turboelectric and mechanical approaches considered for STARC–ABL and ST–ABL, respectively. One option would be an EAP system separate from the main propulsion system that is dedicated to just the BLI propulsor. This system could be powered by onboard stored energy in the form of batteries or a fuel cell system. A battery system would likely be infeasible without significant improvement in battery specific energy relative to the current state of the art. Fuel cells provide much better specific energy (for long mission duration) but would still introduce a significant weight penalty to the configuration. Compared to turboelectric, a fuel-cell-based system has an advantage in that the electricity can be produced at a higher efficiency. Whether or not the efficiency advantage offsets the weight penalty would determine whether this approach is more attractive than the approach taken in STARC–ABL.

The unconventional propulsion architecture of STARC–ABL could also be combined with other advanced configuration concepts. For example, using an airframe with high aerodynamic efficiency, such as the transonic truss-braced wing, could mitigate the impact of the weight added by the electrical components. The ability of the generators in the underwing engines to also function as motors can be leveraged to allow onboard battery storage to add power to the turbofans in some portions of the flight envelope. An example is to allow the engine core to be sized for peak efficiency during cruise with battery power supplementing the core at RTO to produce the necessary thrust. During portions of the flight where the batteries are not being used, power from the generators, in addition to driving the BLI propulsor, can be used to recharge the batteries in the event battery power is needed in an emergency situation such as a refused landing and climb out.

Appendix—Nomenclature

A	cross-sectional area of the cable
hp	horsepower
I	current in amps
K	technology factor
L	length of the cable from generator to tailcone thruster motor and back to generator
P	power
P_{BLI}	power required for the BLI configuration
$P_{\text{free-flier}}$	power required for a reference, free-stream propulsor
P_{loss}	power loss in cable
PSC	power savings coefficient
Pt_0	free-stream total pressure
Pt_3	compressor exit total pressure
R	resistance of the cable
R_s	specific resistivity
rpm	revolutions per minute
Tt_3	compressor exit total temperature
$Tt_{3\text{max}}$	maximum compressor exit total temperature
Tt_4	burner exit temperature
V	voltage
Wc_3	compressor exit corrected flow
$Wc_{3\text{min}}$	minimum value of compressor exit corrected flow

Abbreviations

AATT	Advanced Air Transport Technology
AC	alternating current
ADP	aerodynamic design point
ANOPP	Aircraft Noise Prediction Program
BLI	boundary layer ingestion
CFD	computational fluid dynamics
DC	direct current
EAP	electrified aircraft propulsion
EPNL	effective perceived noise level
FLOPS	Flight Optimization System (aircraft sizing and mission analysis application)
HEATheR	High-efficiency Electric Aircraft Thermal Research
HPC	high-pressure compressor
HPT	high-pressure turbine
L/D	lift over drag ratio
LPC	low-pressure compressor
LPT	low-pressure turbine
MDP	multidesign point
MEA	more electrical aircraft
N3CC	N+3 (technology level) conventional configuration (aircraft)
NPSS	Numerical Propulsion System Simulation
OEI	one-engine inoperative

OpenVSP	Open Vehicle Sketch Pad
OPR	overall pressure ratio (= Pt_3/Pt_0)
PAI	propulsion-airframe integration
PEGASUS	Parallel Electric-Gas Architecture With Synergistic Utilization Scheme
RTO	rolling-takeoff (flight condition)
SLS	sea-level static (flight condition)
ST–ABL	single-aisle transport aircraft with aft boundary layer propulsion
STARC–ABL	single-aisle turboelectric aircraft with aft boundary layer propulsion
SUGAR	Subsonic Ultra Green Aircraft Research
TMS	thermal management system
TOC	top of climb (flight condition)
TRL	technology readiness level
TSFC	thrust-specific fuel consumption
WATE++	Weight Analysis of Turbine Engines—turbine engine weight and flow path application implemented in NPSS

References

1. Lents, C.E., et al.: Parallel Hybrid Gas-Electric Geared Turbofan Engine Conceptual Design and Benefits Analysis. AIAA 2016–4610, 2016.
2. Felder, J.L.; Tong, M.T.; and Chu, J.: Sensitivity of Mission Energy Consumption to Turboelectric Distributed Propulsion Design Assumptions and the N3–X Hybrid Wing Body Aircraft. AIAA 2012–3701, 2012.
3. Capristan, F.M.; and Blaesser, N.J.: Analysis of the Parallel Electric-Gas Architecture With Synergistic Utilization Scheme (PEGASUS) Concept. NASA/TM—2019-220396, 2019. https://ntrs.nasa.gov
4. Borer, N.K., et al.: Design and Performance of the NASA SCEPTOR Distributed Electric Propulsion Flight Demonstrator. AIAA 2016–3920, 2016.
5. Drela, M.: Development of the D8 Transport Configuration. AIAA 2011–3970, 2011.
6. Ordaz, I., et al.: Mitigation of Engine Inlet Distortion Through Adjoint-Based Design. AIAA 2017–3410, 2017.
7. Gray, J.S., et al.: Coupled Aeropropulsive Optimization of a Three-Dimensional Boundary-Layer Ingestion Propulsor Considering Inlet Distortion. J. Aircr., vol. 57, no. 6, 2020, pp. 1014–1025.
8. Welstead, J.; and Felder, J.L.: Conceptual Design of a Single-Aisle Turboelectric Commercial Transport With Fuselage Boundary Layer Ingestion. AIAA 2016–1027, 2016.
9. Samuelsson, Sebastion; and Grönstedt, Tomas: Performance Analysis of Turbo-Electric Propulsion System With Fuselage Boundary Layer Ingestion. Aerosp. Sci. Technol., vol. 109, no. 106412, 2021.
10. Giannakakis, Panagiotis, et al.: Fuel Burn Evaluation of a Turbo-Electric Propulsive Fuselage Aircraft. AIAA 2019–4181, 2019.
11. Schnell, Rainer, et al.: Assessment of a Turbo-Electric Aircraft Configuration With Aft-Propulsion Using Boundary Layer Ingestion. Aerospace, vol. 6, no. 12, 2019.
12 Bijewitz, J.; Seitz, A.; and Hornung, M.: Extended Design Studies for a Mechanically Driven Propulsive Fuselage Aircraft Concept. 2018 AIAA Aerospace Sciences Meeting, AIAA 2018–0408, 2018.
13. Bradley, M.K.; and Droney, C.K.: Subsonic Ultra Green Aircraft Research: Phase I Final Report. NASA/CR—2011-216847, 2011. https://ntrs.nasa.gov
14. Boeing: Spreading Our Wings: Boeing Unveils New Transonic Truss-Braced Wing. 2019. https://www.boeing.com/features/2019/01/spreading-our-wings-01-19. Accessed December 2020.
15. Bradley, M.K., et al.: SUGAR Phase 1 Final Review. 2010. http://aviationweek.typepad.com/files/boeing_sugar_phase_i_final_review_v5.pdf Accessed April 2021.
16 Bradley, M.K.; Droney, C.K.; and Allen, T.: Boeing N+3 SUGAR: Final Update Presentation. Unpublished, 2021.
17 Bradley, M.K.; Droney, C.K.; and Allen, T.J.: Subsonic Ultra Green Aircraft Research Phase II: Truss Braced Wing Design Exploration. NASA/CR—2015-218704/VOL I, 2015. https://ntrs.nasa.gov
18 Bradley, M.K.; and Droney, C.K.: Subsonic Ultra Green Aircraft Research Phase II: Hybrid Electric Design Exploration. NASA/CR—2015-218704/VOL II, 2015. https://ntrs.nasa.gov
19 Jones, S.M.; Haller, W.J.; and Tong, M.T.: An N+3 Technology Level Reference Propulsion System. NASA/TM—2017-219501, 2017. https://ntrs.nasa.gov
20. Elmiligui, A.A., et al.: Numerical Investigation of a Fuselage Boundary Layer Ingestion Propulsion Concept. AIAA 2013–4402, 2013.

21. Bradley, M.K.; and Droney, C.K.: Subsonic Ultra Green Aircraft Research: Phase II: N+4 Advanced Concept Development. NASA/CR—2012-217556, 2012. https://ntrs.nasa.gov

22. Jones, S.M.: An Introduction to Thermodynamic Performance Analysis of Gas Turbine Engine Cycles Using the Numerical Propulsion System Simulation Code. NASA/TM—2007-214690, 2007. https://ntrs.nasa.gov

23. National Aeronautics and Space Administration: NPSS: Numerical Propulsion System Simulation. Consortium Software Package, Version 2.6, 2013.

24. Smith, L.H.: Wake Ingestion Propulsion Benefit. J. Propuls. Power, vol. 9, no. 1, 1993, pp. 74–82.

25. Gray, J.S.; and Martins, J.R.R.A.: Coupled Aeropropulsive Design Optimization of a Boundary-Layer Ingestion Propulsor. Aeronaut. J., vol. 123, no. 1259, 2019, pp. 121–137.

26. Ahuja, Jai; and Mavris, Dimitri N.: A Method for Modeling the Aero-Propulsive Coupling Characteristics of BLI Aircraft in Conceptual Design. AIAA 2021–0112, 2021.

27. Zhang, D., et al.: Development of Megawatt-Scale Medium-Voltage High Efficiency High Power Density Power Converters for Aircraft Hybrid-Electric Propulsion Systems. AIAA 2018–5007, 2018.

28. Husain, E.; and Nema, R.S.: Analysis of Paschen Curves for Air, N2 and SF6 Using the Townsend Breakdown Equation. IEEE Trans. Electr. Insul., vol. EI–17, no. 4, 1982, pp. 350–353.

29. Schnulo, S.L., et al.: Assessment of the Impact of an Advanced Power System on a Turboelectric Single-Aisle Concept Aircraft. AIAA 2020–3548, 2020.

30. Tong, M.T.; and Naylor, B.A.: An Object-Oriented Computer Code for Aircraft Engine Weight Estimation. ASME GT2008–50062, 2008.

31. Brown, G.V.; Kascak, A.F.; and Ebihara, E.: NASA Glenn Research Center Program in High Power Density Motors for Aeropropulsion. NASA/TM—2005-213800, 2005. https://ntrs.nasa.gov

32. Hahn, A.S.: Vehicle Sketch Pad: A Parametric Geometry Modeler for Conceptual Aircraft Design. AIAA 2010–657, 2010.

33. McCullers, L.: Aircraft Configuration Optimization Including Optimized Flight Profiles. Proceedings of the Symposium on Recent Experiences in Multidisciplinary Analysis and Optimization, NASA CP–2327, 1984. https://ntrs.nasa.gov

34. International Civil Aviation Organization: Annex 16 to the Convention on International Civil Aviation. Vol. I: Aircraft Noise. International Standards and Recommended Practices— Environmental Protection, 7th ed., Montreal, 2014.

35. Gillian, R.E.: Aircraft Noise Prediction Program User's Manual. NASA TM–84486, 1982. https://ntrs.nasa.gov

36. Zorumski, W.E.: Aircraft Noise Prediction Program Theoretical Manual, Parts 1 and 2. NASA TM–83199, 1982. https://ntrs.nasa.gov

37. Stone, J.R., et al.: Jet Noise Modeling for Suppressed and Unsuppressed Aircraft in Simulated Flight. NASA/TM—2009-215524, 2009. https://ntrs.nasa.gov

38. Kontos, K.B.; Janardan, B.A.; and Gliebe, P.R.: Improved NASA–ANOPP Noise Prediction Computer Code for Advanced Subsonic Propulsion Systems, Volume 1: ANOPP Evaluation and Fan Noise Model Improvement. NASA CR–195480, 1996. https://ntrs.nasa.gov

39. Emmerling, J.J.; Kazin, S.B.; and Matta, R.K.: Core Engine Noise Control Program. Vol. III, Supplement 1-Prediction Methods. FAA RD–74–125, III–I, March 1976.

40. Kontos, K.B.; Kraft, R.E.; and Gliebe, P.R.: Improved NASA–ANOPP Noise Prediction Computer Code for Advanced Subsonic Propulsion Systems, Volume 2: Fan Suppression Model Development. NASA CR–202309, 1996. https://ntrs.nasa.gov

41. Guo, Y.: Empirical Prediction of Aircraft Landing Gear Noise. NASA/CR—2005-213780, 2005. https://ntrs.nasa.gov

42. Fink, M.R.: Airframe Noise Prediction Method. FAA RD–77–29, March 1977.

43. Clark, I.A.; Thomas, R.H; and Guo, Y.: Aircraft System Noise Assessment of the NASA D8 Subsonic Transport Concept. AIAA 2018–3124, 2018.

44. Society of Automotive Engineers: Standard Values of Atmospheric Absorption as a Function of Temperature and Humidity. Aerospace Recommended Practice 866A, 1975.

45. Chien, C.; and Soroka, W.W.: Sound Propagation Along an Impedance Plane. J. Sound Vib., vol. 43, no. 1, 1975, pp. 9–20.

46. Embleton, T.F.W.; Piercy, J.E.; and Daigle, G.A.: Effective Flow Resistivity of Ground Surfaces Determined by Acoustical Measurements. J. Acoust. Soc. Am., vol. 74, no. 4, 1983, pp. 1239–1244.

47. Perullo, C., et al.: Cycle Selection and Sizing of a Single-Aisle Transport With the Electrically Variable Engine (EVE) for Fleet Level Fuel Optimization. AIAA 2017–1923, 2017.

48 Georgia State University: Resistivity and Temperature Coefficient at 20 C. Table, HyperPhysics. http://hyperphysics.phy-astr.gsu.edu/hbase/Tables/rstiv.html Accessed April 2021.